The International Journal of Advanced Manufacturing Technology (2024) 133:2967–2994
https://doi.org/10.1007/s00170-024-13980-3

ORIGINAL ARTICLE

Kinematics characterizing with dual quaternion and parametric modeling of geometric error terms based on measuring path planning of CNC machine tools

Shijie Guo[1,2] · Yunhe Zou[1] · Wangwang Huang[2] · Shufeng Tang[1] · Xuesong Mei[2]

Received: 10 April 2024 / Accepted: 2 June 2024 / Published online: 12 June 2024

Abstract
Geometric error is a crucial factor influencing the spatial accuracy of CNC machine tools. A novel methodology for modeling, measuring, and identifying geometric errors in multi-axis machine tools is proposed in this paper. Firstly, a synthetic volumetric error model is established by utilizing dual quaternions for multi-axis CNC machine tools. To characterize the relative position relationship between the tool and the workpiece, the kinematics model automatically incorporates the complex coupling between position and orientation motion in an implicit way, enabling a concise and compact representation of the kinematics. Secondly, measure path planning includes candidate measurement positions which are screened to obtain the optimal position group by using observation indices and the modified Detmax method. Thirdly, a parametric modeling method based on exponential cosine fitting is proposed for representing both angular and linear errors, and an improved sparrow search algorithm and nested parameter uncertainty optimization are established to process curve fitting–based optimization of the geometric error term. The fitting of the exponential cosine model is quantified with model uncertainty, and the nested uncertainty optimization method is employed to improve geometric error terms with a poor fitting effect. Finally, the effectiveness is demonstrated through experimental comparisons. The geometric error of a single axis has an average decreased of 69.7%, and the compensation rate of roundness driven by two-axis synchronization is an average of 68.7%. This method offers the advantage of quantifying the minimum optimal number of measurements and positions, improving the efficiency of parametric modeling.

Keywords CNC machine tools · Geometric error · Dual quaternion · Measuring path planning · Parametric modeling

1 Introduction

High-precision manufacturing has emerged as an unavoidable trend in the ongoing evolution of the equipment manufacturing industry [1, 2]. Industries such as aviation, automotive, and medical manufacturing are placing ever-growing demands on machine tool manufacturing for high precision and efficiency. As intelligent design and precision machining technology rapidly advance, the design and manufacturing accuracy of components have seen significant enhancements, and the geometric accuracy now pervades the entire manufacturing process of machine tools and stands as a pivotal factor in determining the quality of machine tool accuracy [3, 4]. The significance of error compensation in guaranteeing machining accuracy on CNC machine tools and optimizing the performance of in-service machine tools is steadily gaining prominence [5]. Therefore, improving the quasi-static accuracy of the machine tool has become a research focus of the machine tool manufacturing industry today.

Geometric error serves as a quantitative indicator reflecting quasi-static accuracy, and these errors can be classified into two types: position-dependent geometric errors (PDGEs) and position-independent geometric errors (PIGEs) [6, 7]. PDGEs are mainly caused by manufacturing defects in the feed system itself, while PIGEs are mainly caused by the assembling of machine tool manufacturers [8]. PDGEs are

✉ Yunhe Zou
yhzouimut@163.com

[1] The College of Mechanical Engineering, Inner Mongolia University of Technology, Hohhot, People's Republic of China 010051

[2] School of Mechanical Engineering, State Key Laboratory for Manufacturing Systems Engineering, Xi'an Jiaotong University, Xi'an, People's Republic of China 710049

referred to as component errors according to ISO 230–7 [9]; scholars have also proposed many similar terms to define PIGEs, such as location error, link error parameter, kinematic error, and systematic deviation [10]. Geometric errors are related to the shape and position accuracy of machine tool components, with good repeatability, strong quasi-static characteristics, and high systematicity. The influence of geometric errors on machine tool accuracy will be more significant when the environmental temperature with a little fluctuation [11]. Therefore, to address geometric errors by adopting a systematic approach for improving, the accuracy of CNC machine tools has become a crucial problem. Error compensation is more suitable for improving accuracy in the process of application of machine tools compared to error prevention [12]; a modeling method effectively and succinctly, precise measurement and identification scheme, and parameterized representation of the error element are the core of constructing error compensation strategies.

Geometric error modeling serves as the cornerstone of error compensation technology, which includes two components: error synthesis modeling and error term parameterization modeling. Establishing an error comprehensive model is a prerequisite for error measuring and compensating of each error term, and parameterized modeling of individual errors is a means to achieve error characterization. The motion chain of the machine tool is abstracted into a multi-body system, and its motion characteristics can be described based on kinematic theory. The conventional methods for establishing error synthesis models include the D-H method, homogeneous transformation matrices (HTMs), and the multi-body system theory method [13]. Some novel modeling methods have been adopted which include screw theory, differential motion matrix method, dual quaternions, and so on. Ding et al. [14] proposed a summation operation rule for geometric error modeling based on the HTM method, in which higher-order error terms are avoided effectively by using a summation operator. Chen et al. [15] constructed the positional relationship between the ideal coordinate vector and the actual coordinate vector of the motion axis under the combined influence of linear and angular errors and proposed an error expression for the single-axis screw transformation matrix based on the screw theory. Chen et al. [16] developed a modeling method based on the improved Jacobian-Torsor method to describe the relationship between the machining geometric tolerance range, and the continuous expression of non-uniformly distributed of geometric errors at different motion positions in the spatial domain was proposed. Yao et al. [17] presented the measurement error model consisting of a toolchain and workpiece chain by using the dual quaternion, which reduces the computational time and calculation costs of matrix multiplication. Fu et al. [18] established a vector component expression function for positional independent geometric errors of the double rotary table type five-axis machine tool based on the exponential product theory. The NURBS curves have strong local control ability on control points, which can achieve high-precision fitting of irregular data of geometric error elements [19]. Peng et al. [20] characterized the curve shape of PDGEs with a limited number of control points, PDGEs are fitted into B-spline curves, and the PDGE of the rotation axis is identified through unbounded constraint optimization algorithms. Tian et al. [21] established a high-order polynomial model of PDGEs of a three-axis machine tool, and the order of the polynomial model is determined through the ridge regression method. Fan et al. [22] adopted orthogonal polynomials to express the geometric error term, and the fitting accuracy of the geometric error term was improved by transforming orthogonal polynomial fitting into a multi-linear regression problem. Dual quaternions evolved from even numbers theory and quaternions theory, due to the advantages of considering both the rotary and translate motion of rigid bodies and high computational efficiency, which have been widely used in fields such as robot kinematics, inertial navigation, spacecraft rendezvous and attitude determination, and biomedical. Dual quaternions are the most efficient and compact method for expressing screw displacement in terms of expression and computational efficiency compared with screw theory [23]. The general motion of a rigid body in space can be represented by helical motion based on Chasles' theory, which makes it an effective tool for describing spiral motion and performing pose transformations. It offers advantages such as clear physical meaning, fewer parameters, global singularity-free representation, and a concise and compact form [24].

Compared to the homogeneous transformation matrix method, the screw theory and exponential product formula modeling methods only require the establishment of the tool workpiece and reference coordinate system without more local coordinate systems needing to be established; however, the matrix multiplication method is still used in the calculation process, which is more complex in representation and has lower computational efficiency. Therefore, it is necessary to propose a geometric error model that is concise in representation and computationally efficient. For the modeling of geometric error terms, the polynomial fitting form is simple relatively, and with the degree gradually increases of polynomial, the fitting effect improves gradually. However, there are still some areas that need to be processed: (1) polynomial fitting will result in unstable results when ill-conditioned matrices have the potential to appear during solving; (2) the conventional fitting evaluation parameters cannot characterize the distribution of deviation between predicted and actual values with small numerical differences, and further optimization of the model is needed when the fitting effect of the model is poor.

Geometric error measurement and identification are the core of error compensation technology; the geometric error of machine tools can be measured for each motion axis directly, which can also be measured using calibrated workpieces indirectly, machined workpieces [25]. The indirect measurement method is to obtain the comprehensive error of the machine tool through the multi-axis motion synchronously and then obtain the individual error through mathematical methods [26]. It is often achieved through machining testing or setting preset trajectories for error decoupling [27]. The direct measurement method involves measuring the geometric error of a single axis using standard samples such as ball and disk arrays, rulers, goniometers, and step gauges directly. In this method, all motion axes remain stationary except for the one that needs to be measured. This method is directly influenced by the accuracy of the benchmark and is influenced by external factors such as external forces and temperature, which can cause changes in the dimensional and geometric tolerance of the standard [28], resulting in measurement errors and uncertainty in the results. Among the direct and indirect measurement methods mentioned above, laser interferometers, laser trackers, and tracking interferometers are commonly used as specialized instruments that can calibrate the accuracy of machine tools based on the principle of linear propagation and the wavelength of light [29, 30]. Maruyama et al. [31] and Ibaraki et al. [32] proposed a scheme in just one laser interferometer based on a set of distance measurements to identify all two-dimensional PDGEs of two linear axes in a plane. To measure the positioning error of two linear axes directly, it is also possible to identify the two-dimensional error motion of two linear axes by conducting only one tracking test. Peng established three non-collinear measurement paths for identifying the six geometric errors of the linear axis of the machine tool; the optimal installation parameters were obtained based on sensitivity analysis and studied the impact of each installation parameter on the identification results [33]. Zhang et al. [34] proposed a modeling method for the spatial geometric error of CNC machine tools based on analyzing the principle of two-dimensional angle error, and a laser Doppler interferometer was used to measure the diagonal error of CNC machine tools before and after compensation. Tang et al. [35] used the 12-line method with a Renishaw laser interferometer to measure and identify five PDGEs on each linear axis of the multi-axis grinding machine except for rolling errors, and six PDGEs of the rotary axis are identified by using DBB indirectly. Zhong et al. [36] proposed a new method for measuring and identifying squareness errors in multi-axis machine tools based on the XM-60 interferometer, which solves the problem of inaccurate measurement results caused by geometric error coupling between the two motion axes.

Optimizing measurement paths or constructing redundant measurement schemes are effective methods for enhancing the precision and efficiency of geometric error measurements. Brosed et al. [37] proposed a precision calibration model for machine tools with a telescopic rod. Interference sensors are utilized to automatically track targets for distance measurement. Simultaneously, three high-precision telescopic instruments are used for multipoint positioning and optimized using uncertainty estimation. Data collection time is reduced, and measurement accuracy is enhanced. Experimental results demonstrate the effectiveness of this equipment and method for calibrating machine tool precision. Zhou et al. [38] utilized the condition number of the identification matrix to describe the perturbation of motion parameters using the DBB continuous path. Constrained by the feasibility and collision-free requirements of measuring positions, measurement trajectories based on two-parameter splines were constructed; continuous measurements without collisions or abrupt changes are achieved. Wang et al. [39] proposed a synchronized motion trajectory measurement method based on DBB with dual rotating axes. To address the asynchrony between data sampling and motion during DBB movement, a spherical measurement trajectory was constructed by directly balancing trajectory lengths. Additionally, a synchronization matching algorithm between the ball bar instrument sampling and machine tool motion was proposed to resolve issues such as variations in the distance between the two bases and asynchronous relative motion speeds during the ball bar instrument's trajectory. These advancements effectively enhanced the precision of error detection experiments. Yang et al. [40] established the root mean square error of the geometric error sensitivity coefficients for the rotary axis, and a functional relationship between the root mean square error and the workpiece geometric error in cylindrical coordinates was established. Subsequently, utilizing an adaptive algorithm, these coefficients were minimized, thereby determining the optimal measurement path for the R-test. Xu et al. [41] proposed a measurement approach for dual five-axis machine tools that combines R-testing with milling head motion, support head motion, and synchronous motion trajectories. By transforming the quasi-static and dynamic measurement data from these three different trajectories into a unified reference coordinate system, a measurement process that only requires the installation of an R-test once is achieved. This effectively avoids the time-consuming repetitive installation and calibration processes, while also reducing the influence of installation errors on the results. Additionally, this method enables the identification of dynamic errors in PIGEs and rotary axes. Xu et al. [42] proposed a universal identification model for position-dependent geometric errors of the rotary axis based on single-axis drive. The feasibility of the identification model is determined by the rank of the identification

matrix, and a variable-height trajectory measurement pattern is constructed to achieve stable identification of position-independent geometric errors.

As the most effective specialized instrument for measuring geometric errors for machine tools, laser interferometers have two different measurement methods when measuring straightness errors, which is entirely dependent on relative motion between the interferometer and reflector. The coupling components of angle error do not include measurement data of straightness when the reflector is fixed and the interferometer moves, due to the interferometer being a Wollaston prism and not affected by vertical angle changes. If the interferometer is fixed and the reflector is moved, the reflector is more sensitive to changes in the pitch angle generated by the vertical direction of the machine tool. When an extremely small pitch angle is generated by the reflector, the length of the incident and reflected light between the interferometer and the reflector will also change relatively. Therefore, a small nonlinearity value will be coupled in the straightness error data, which is a function of the distance between optical arrays and the pitch angle. This means that there is error coupling in the measurement and identification by using a laser interferometer measurement. Besides, some current drawbacks of geometric error measurement need to be improved exist as follows: (1) Better parameter estimation can be further achieved through redundant measurement, but it reduces measurement efficiency and introduces uncertainty caused by installation; (2) the formation of a measurement position matrix based on the identification equation focuses more on the non-singularity of the matrix; the impact of different measurement position combinations on measurement and identification accuracy was not be considered comprehensively.

The advantages in this paper are listed as follows: (1) A new error modeling is proposed for multi-axis CNC machine tools in the global coordinate system based on dual quaternions, achieving spatial transformation of geometric error terms without singular representation in Euclidean space. (2) Parametric modeling is implemented, and the fitting accuracy of error terms is optimized based on the evaluation of uncertainty. (3) Optimal measuring points are proposed to ensure identification accuracy through selection based on the quantity of measurements and measurement locations, rather than simply constructing non-singular matrices or selecting measurement positions blindly.

The structure of the paper is as follows: Sect. 2 "Geometric error modeling based on dual quaternion" introduces dual quaternion representations of PIGEs, and PDGEs for multi-axis CNC machine tools were constructed, and a comprehensive error model for multi-axis CNC machine tools was established using dual quaternion in the global coordinate system. Section 3 "Geometric error measuring and identification" introduces the measurement path and identification method for geometric errors of linear axes are established errors. Section 4 "Parametric modeling of geometric error terms and uncertainty optimization" introduces the method of parametric modeling and uncertainty optimization. Section 5 "Case study" introduces experiments on a three-axis precision machine to verify the effectiveness of modeling, measurement, and identification, as well as the compensation. Section 6 "Conclusion" concludes the main findings and conclusions of this research, the disadvantages, and future research direction.

2 Geometric error modeling based on dual quaternion

2.1 Basic theory of dual quaternion

The rotary and translation vectors are not the exclusive expressions of rigid body motion in three dimensions, nor are they the sole representations of linear transformations. A more effective method for representing spiral motion involves utilizing dual quaternions to express spatial points, which can also be employed for motion parameter calculations. Any pair of dual numbers in the distributed domain is

$$\hat{a} = a + \varepsilon a_0 \tag{1}$$

where a is the real part of the dual number, a_0 is the dual part of the dual number, and ε is the dual operator. The conjugation of the dual number is

$$\overline{a} = a - \varepsilon a_0 \tag{2}$$

Dual numbers can be expressed as a function obtained through Taylor expansion:

$$\begin{aligned} f\left(a + \varepsilon a_0\right) &= f(a) + \varepsilon a_0 f\prime(a) + \varepsilon^2 \tfrac{a_0^2}{2!} f''(a) + \cdots \\ &= f(a) + \varepsilon a_0 f\prime(a) \end{aligned} \tag{3}$$

Quaternion is an extension of complex numbers on the four-dimensional real space $\mathbb{R}^4$. The set of quaternions is denoted as

$$\mathbb{N} = \left\{ \mathbf{q} : \mathbf{q} = q_0 + q_1 i + q_2 j + q_3 k, q_0, q_1, q_2, q_3 \in \mathbb{R} \right\} \tag{4}$$

where i, j, and k are complex units, and a more compact expression of quaternion is

$$\mathbf{q} = \left[q_0, q_1, q_2, q_3\right]^{\mathrm{T}} = \left[q_0, \boldsymbol{q}^{\mathrm{T}}\right]^{\mathrm{T}} \tag{5}$$

where q_0 and $\boldsymbol{q} = \left[q_1, q_2, q_3\right]^{\mathrm{T}}$ are referred to as the scalar and vector parts of quaternions, respectively.

The relative orientation between two coordinate systems can be described with unit quaternion, as well as the projection of vector in different coordinate systems. For

example, q_{xy} represents the quaternion of F_x coordinate system relative to F_y coordinate system. For any three-dimensional vector $a \in \mathbb{R}^3$, the relationship between its coordinate projection a^x in F_x and its coordinate projection a^y in F_y is

$$\boldsymbol{a}^x = q_{xy}^* \otimes a^y \otimes q_{xy} \tag{6}$$

Two quaternions and one dual unit of dual quaternions are as follows:

$$\begin{aligned} \hat{q} &= \dot{q}_r + \varepsilon \dot{q}_t \\ \dot{q}_r = \dot{q}_{\delta \mathbf{n}} &= \left[s_r v_r \right]^{\mathrm{T}} = \begin{bmatrix} sin\left(\frac{\theta}{2}\right) n \\ cos\left(\frac{\theta}{2}\right) \end{bmatrix} \\ \dot{q}_t &= \left[s_t \ v_t \right]^{\mathrm{T}} = \frac{1}{2} t \circ \dot{q}_{\delta \mathbf{n}} \end{aligned} \tag{7}$$

where $\dot{q}_r$ is the real part of a dual quaternion, representing rotary transformation; n is the unit direction vector which is the rotary transformation; θ is the rotary angle; $\dot{q}_t$ is the imaginary part of a dual quaternion, representing a linear transformation; and t is the vector of the displacement transformation. The spiral motion of the coordinate system represented by the unit dual quaternion $\hat{q}$ is shown in Fig. 1.

Dual quaternions can also be defined as dual angles $\hat{\theta}$, in addition to being in the form of Eq. 8, and the dual vector $\hat{l}$ of the spiral axis is

$$\hat{q} = \left[cos\left(\frac{\hat{\theta}}{2}\right) sin\left(\frac{\hat{\theta}}{2}\right) \hat{l} \right]^T \tag{8}$$

where

$$\begin{cases} \hat{\boldsymbol{\theta}} = \theta + \varepsilon d \\ \hat{\boldsymbol{l}} = l + \varepsilon (\boldsymbol{l} \times p) \end{cases} \tag{9}$$

where p represents the position vector of any point p on the rotary axis l.

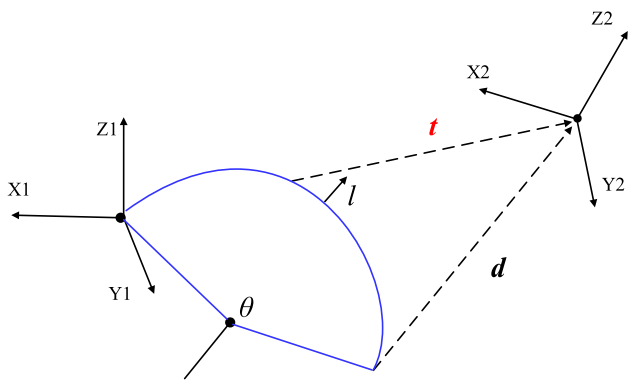

Fig. 1 Spiral motion of the coordinate system

The expansion of Eq. 7 is represented as two quaternions, and the rotary quaternion and translation quaternion can be expressed as

$$\dot{q}_r = \begin{bmatrix} sin\left(\frac{\delta}{2}\right) \mathbf{n}_\delta \\ cos\left(\frac{\delta}{2}\right) \end{bmatrix} \tag{10}$$

$$\dot{q}_t = \begin{bmatrix} \frac{d}{2} cos\left(\frac{\delta}{2}\right) \mathbf{n}_\delta + msin\left(\frac{\delta}{2}\right) \\ -\frac{d}{2} sin\left(\frac{\delta}{2}\right) \end{bmatrix} \tag{11}$$

where d, n, and m are the four relevant parameters of screw theory; n represents the unit vector of the rotary axis; δ is the rotary angle; $d = t \cdot n_\delta$ is the displacement along the rotary axis, and $m = (p \times n_\delta)$ is the torque vector of the rotary axis relative to the origin of the reference coordinate system.

After the n-th iteration of spiral motion of the motion axis, the spatial transformation of Plücker lines from the i-th coordinate system to the $(i+1)$-th coordinate system can be expressed as

$$\hat{l}^{i+1} = \mathfrak{R}\left(\hat{q}^i_{(tn\delta)}\right) \circ \hat{l}^i = \hat{q}^i_{(tn\delta)} \circ \hat{l}^i \circ \hat{q}^{i}_{(tn\delta)} * \tag{12}$$

The utilization of dual quaternions effectively circumvented multiplication operations between matrices in error modeling, leading to reduced computational time and clearer expression.

2.2 Modeling of volumetric errors of multi-*axis* machine tool

For multi-axis CNC machine tool based on the rigid body assumption, each motion axis has 6 degrees of freedom in its motion space; therefore, each motion axis has 6 PDGEs. There is a difference in the representation of PIGEs between motion axes. In accordance with ISO 230–1 standards [43], the PIGEs and PDGEs of the machine tool are displayed in Table 1, represented using dual quaternions.

The three-axis machine tool consists of *X*-, *Y*-, *Z*-, and spindle-axes. The cutting tool at the end of the tool chain, the workbench at the end of the workpiece chain, and the schematic and structure of the machine tool are shown in Fig. 2.

Table 1 Geometric errors of three-axis machine tool

Motion axis	PDGEs		PIGEs
	Linear error	Angle error	Angle error
X-axis	E_{XX}, E_{YX}, E_{ZX}	E_{AX}, E_{BX}, E_{CX}	E_{C0X}, E_{A0Z}, E_{B0Z}
Y-axis	E_{XY}, E_{YY}, E_{ZY}	E_{AY}, E_{BY}, E_{CY}	
Z-axis	E_{XZ}, E_{YZ}, E_{ZZ}	E_{AZ}, E_{BZ}, E_{CZ}	

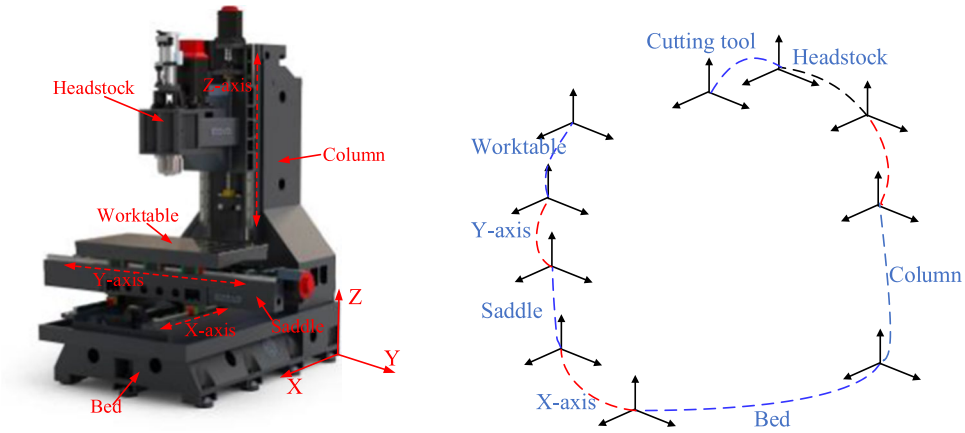

Fig. 2 Machine tool schematic and kinematic chain

Table 2 Plücker line representation for each motion axis

Coordinate system	n_{δ}^{i}	t^{i}	m^{i}
X	$[100]^{\mathrm{T}}$	$[000]^{\mathrm{T}}$	$[000]^{\mathrm{T}}$
Y	$[010]^{\mathrm{T}}$	$[000]^{\mathrm{T}}$	$[000]^{\mathrm{T}}$
Z	$[001]^{\mathrm{T}}$	$[000]^{\mathrm{T}}$	$[000]^{\mathrm{T}}$
WCS	$[010]^{\mathrm{T}}$	$[x_w y_w z_w]^{\mathrm{T}}$	$[z_w 0 - x_w]^{\mathrm{T}}$
TCS	$[010]^{\mathrm{T}}$	$[x_t y_t z_t]^{\mathrm{T}}$	$[z_t 0 - x_t]^{\mathrm{T}}$

The reference coordinate system was established as for describing the spatial positions. The tool coordinate system *TCS* and the workpiece coordinate system *WCS* are located on the tool tip and workpiece, respectively. The coordinate system of the *X*-, *Y*-, and *Z*-axes of the CNC machine tool is defined by ISO 230-1 as Cartesian coordinate system.

The orientation of the Plücker line representation for each motion axis is based on the reference coordinate system of the machine tool, and the representation method of the Plücker line is detailed in Table 2.

Where x_w, y_w, z_w is the position deviation of the tool coordinate system relative to the machine tool reference system and x_t, y_t, z_t is the position deviation of the WCS relative to the machine tool reference system.

In the two motion chains of a three-axis machine tool, the tool motion chain is represented as the *i*-th motion axis system except for the tool, while the workpiece motion chain is represented as the *j*-th motion axis system except for the tool end. The smaller the values of *i* and *j*, the closer of motion axis is to the tool end and the workpiece end, and $i=3, j=2$.

The models of the tool motion chain and the workpiece motion chain can be obtained respectively based on the spatial position relationship between adjacent axes of the motion chain under ideal motion conditions; the kinematic model of the toolchain is

$$\begin{cases} \hat{t}_l^R = R\left(\hat{q}_{(t\mathbf{n}t)}^{i}\right) \circ R\left(\hat{q}_{(t\mathbf{n}t)}^{i-1}\right) \circ R\left(\hat{q}_{(t\mathbf{n}t)}^{i-2}\right) \circ \hat{t}^{l} \\ \hat{n}_l^R = \hat{n}^{l} \end{cases} \tag{13}$$

The kinematic equation of the workpiece chain is

$$\begin{cases} \hat{t}_w^R = R\left(\hat{q}_{(t\mathbf{n}\delta)}^{j}\right) \circ R\left(\hat{q}_{(t\mathbf{n}\delta)}^{j-1}\right) \circ \hat{t}^{w} \\ \hat{n}_l^R = R\left(\hat{q}_{(\mathbf{n}\delta)}^{j}\right) \circ R\left(\hat{q}_{(\mathbf{n}\delta)}^{j-1}\right) \circ \hat{n}^{w} \end{cases} \tag{14}$$

Based on the principle of dual quaternion space transformation, the Plücker line orientation expression of the actual axis of the machine tool motion axes in the machine tool reference coordinate system is obtained. The Plücker line parameters of the ideal axis in the model are replaced, and the actual motion error model of the machine tool is established. The actual kinematic model with geometric error, representing the workpiece relative to the tool, is denoted as

$$\begin{cases} \hat{t}_w^t = \hat{t}^{l*} \circ R\left(\hat{q}_{(tnt)}^{i-2\,*}\right) \circ R\left(\hat{q}_{(tnt)}^{i-1\,*}\right) \circ R\left(\hat{q}_{(tnt)}^{i\,*}\right) \circ R\left({}_{actual}\hat{q}_{(tnt)}^{j}\right) \circ R\left({}_{actual}\hat{q}_{(tnt)}^{j-1}\right) \hat{t}^{w} \\ \hat{n}_w^t = R\left({}_{actual}\hat{q}_{(n\delta)}^{j}\right) \circ R\left({}_{actual}\hat{q}_{(n\delta)}^{j-1}\right) \hat{n}^{w} \end{cases} \tag{15}$$

The error terms in Table 1 are substituted into the kinematic equation mentioned above, and the kinematic model is expanded as follows:

$$\begin{cases} \Delta_x = -E_{XX} - E_{XY} + E_{XZ} - y \cdot E_{CX} - z \cdot E_{BX} - z \cdot E_{BY} + z \cdot E_{B0Z} + y_T \cdot \left(E_{CX} + E_{CY} \right. \\ \left. -E_{CZ}\right) - z_T \cdot \left(E_{BX} + E_{BY} - E_{BZ}\right) \\ \Delta_y = -E_{YX} - E_{YY} + E_{YZ} + x \cdot E_{CX} + z \cdot E_{AX} + z \cdot E_{AY} + x \cdot E_{C0X} - z \cdot E_{A0Z} - x_T \cdot \\ \left(E_{CX} + E_{CY} - E_{CZ}\right) + z_T \cdot \left(E_{AX} + E_{AY} - E_{AZ}\right) \\ \Delta_z = -E_{ZX} - E_{ZY} + E_{ZZ} - x \cdot E_{BX} + y \cdot E_{AX} + y \cdot E_{AY} + x_T \cdot \left(E_{BX} + E_{BY} - E_{BZ}\right) \\ -y_T \cdot \left(E_{AX} + E_{AY} - E_{AZ}\right) \end{cases} \tag{16}$$

Equation 16 can be further reduced to a more condensed matrix form, as follows:

$$\Delta R = \left[J_i\right]\left[E_i\right] \tag{17}$$

where $[J_i]$ is the identification matrix consists of installation parameters and motion command and $[E_i]$ is the geometric error vector.

Based on the geometric error representation defined by dual quaternions, the geometric error model of the three-axis CNC machine tool is established. Dual quaternions were utilized to represent the singularity-free space transformation in Euclidean space, which only the machine tool coordinate system and workpiece coordinate system require, and local coordinate systems are not required. Hence, the geometric error terms can be expressed in the absolute coordinate system, and this effectively ensures consistency with the definitions of PDGEs within ISO 230–1. The orientation of each motion axis of the machine tool is represented by Plücker, geometric error modeling will be more convenient, and functional relationship expression between the motion axis and the comprehensive orientation will be achieved intuitively.

3 Geometric error measuring and identification

3.1 Optimal selection of measurement quantity

When the quantity of measurement equals the number of error terms to be identified and the identification matrix that $[J_i]$ as expressed in Eq. 17 is not singular, geometric errors can be identified. The optimal selection of measurement quantity is based on the identification matrix of the parameters and motion axis parameters. Specifically, this can be reflected in the observability index of the identification Jacobian matrix. The larger the observability index of the identification matrix, the greater the impact of the machine tool's geometric error terms on the spatial error vector.

Before optimizing measurement positions, it is necessary to determine the minimum quantity of measurements. Observational indices of the identification coefficient matrix can be used to select the measurement position and also to determine the quantity of measurements. The compromise between measurement accuracy and efficiency can be achieved by determining the minimum number of measurements where the identification accuracy is no longer significantly improved. The identification matrix is decomposed by a singular value, and the observability index is listed based on the singular value combination. Subsequently, the optimal number of measurements is selected.

The observability index is defined as the ratio of the minimum to the maximum of all singular values of the discernible Jacobian matrix $[J_i]$, i.e.,

$$O_{\text{in}} = \frac{\gamma_k}{\gamma_{\text{i}}} \tag{18}$$

where γ_i and γ_k are the maximum and minimum values of the singular values of the identification matrix $[J_i]$, respectively.

The observability index is used to optimize the minimum number of optimal measurement positions, denoted as O_{in}, ensuring good performance. This implies that the observability index can converge to the maximum value with fewer measurement positions. When the observability index is 1, it indicates that all singular values of the Jacobian matrix are equal, and the measurement position group exhibits strong observability for geometric error terms.

The steps of optimal selection of measurement quantity are as follows:

1. The initial measurement position set U_1 consists of N_1 randomly selected measurement positions from the complete set of measurement positions UG.
2. The position ψ_i in the set of remaining positions U_r is traversed, and a temporary set U_{N+1}^i is constituted by ψ_i and the set of N measurement positions U_N^A. All the positions in the temporary set are used to compute the identification Jacobian matrix, and then singular value decomposition is performed.

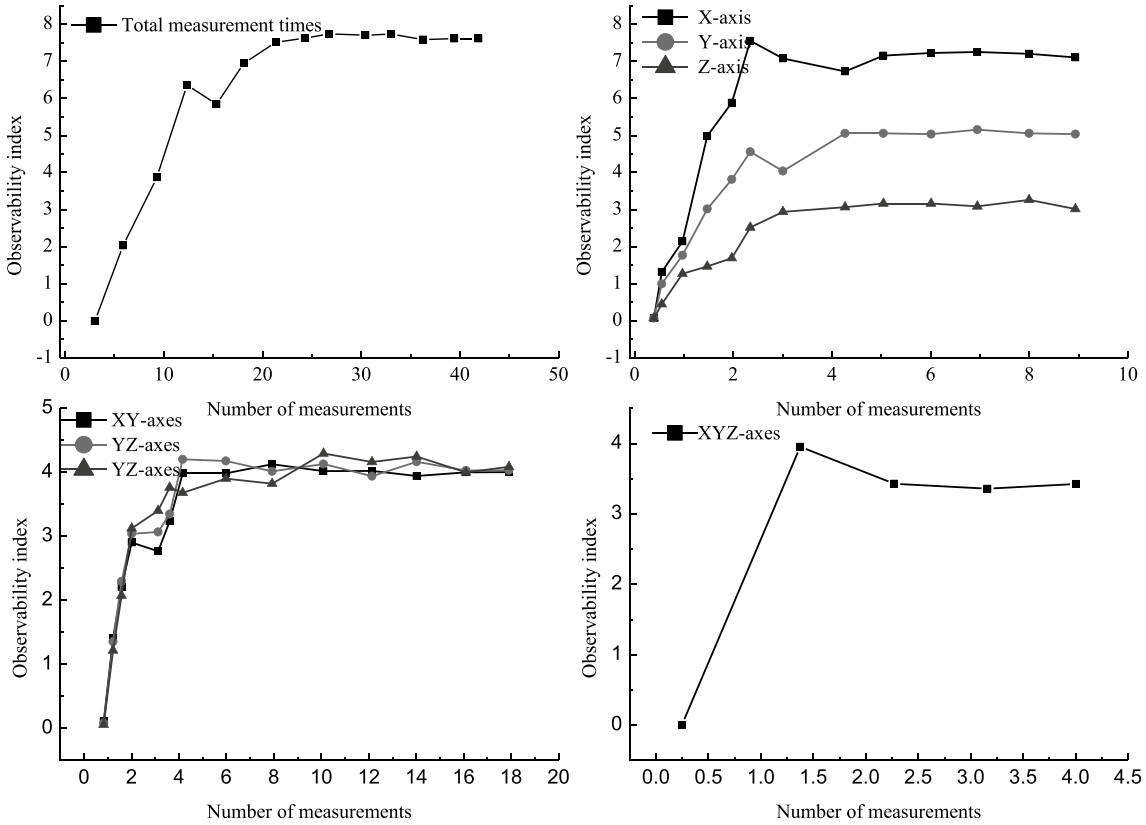

Fig. 3 State curve of the observed index and the quantity of measurements

3. The observability index corresponding to the set is calculated, and the maximum value of the observability index is iteratively and continuously updated. At the same time, the corresponding measurement position is recorded.
4. After the traversal is completed, the position corresponding to the maximum value of the observability index is assigned to ψ^A, and U_{n+1} is established by combining it into a new set U_{N+1}^A along with the existing positions. Simultaneously, a "row block" is added to the identification Jacobian matrix.
5. The addition operation stops when the number of positions in U_1 reaches the specified upper limit.
6. The variation of the observability index can be observed as positions are added. The minimum number of measurement positions, N_r, is determined when there is no significant change in the condition curve.

In the above operation, the measurement points for x, y, and z are located within their respective effective ranges, i.e., $x \in [-300, 300]$, $y \in [-210, 210]$, and $z \in [-260, 260]$ of the identification matrix, with values taken as random points within this range, steps (2) to (4) are defined as additional position operations. The observability index can be obtained through the selection of optimal measurement times, and the condition curve is shown in Fig. 3.

According to the optimization method for number of measurements, the number of measurements is 19, and the observability index did not increase significantly and reached a stable peak; specifically, the number of measurements required for a single motion of the *X*-, *Y*-, *Z*-axes is 5, 4, and 3, respectively; number of measurements of two-axis simultaneous motion for *X*–*Y*, *Y*–*Z*, and *Z*-*X*-axes are assigned twice, and three-axis simultaneous motion needs to be done once.

3.2 Selection of measurement stroke based on modified D-optima

After determining the optimal number of measurements for the motion axis, the direct identification of geometric error terms becomes challenging. Furthermore, the accuracy of machine tool error identification is influenced by varying measurement positions and trajectories. Consequently, screening the measurement positions is imperative to achieve enhanced identification accuracy. The optimal measurement position selection method addresses the challenge of identifying measurement positions reachable by a set of machine tool motion axes, which can minimize interference from unmodeled error sources and measurement disturbances in identifying machine tool geometric error terms.

An improvement strategy to the D-optimal algorithm with a single iteration was proposed to optimize the initial measurement position set. This strategy involves updating positions rather than simply replacing them. Leveraging existing D-optimal algorithm improvement strategies and methods for determining the minimum number of measurement positions, we introduce an Improved D-optimal Algorithm (IDOA) for selecting the minimum optimal measurement positions in this paper. The algorithm process is illustrated in Fig. 3, and the primary steps of IDOA for measuring position optimization are outlined as follows:

1. Initialization: The process begins with the calculation of the initial position number, N_1. Subsequent positions are then assessed until the minimum measurement pose number, N_T, is determined.
2. Random selection: A random combination is employed to choose N_1 measurement positions from the complete set U_G of selected measurement positions. This selection forms the initial measurement position set U_O. Subsequently, multiple remaining measurement position sets, U_{R}, are generated accordingly.
3. Position update operation: Following the execution of additional position selection, the delete position operation is employed to optimize the N_1 positions within the initial measurement set U_O. The delete position operation unfolds as follows: A temporary dataset, U_N^i, is obtained by eliminating ψ^A from the set after traversal U_{N+1}^{A}. The Jacobian matrix for error identification is computed using all positions within the temporary dataset. Subsequently, a singular value decomposition is conducted on this matrix to determine the observability index value pertaining to the set. Continuously, the maximum observability indicator value is updated, and the corresponding pose is concurrently recorded. Upon traversal, the position corresponding to the maximum observability indicator is designated as ψ^R. This position is then removed from the set U_{N+1}^{A} to formulate a fresh set U_N^{R}, while simultaneously removing a "row block" from the identification Jacobian matrix.
4. Add position operation: The additional position operation serves to augment the number of poses within the position set U_O until the minimum required number of measured positions, T_N, as stipulated in step 1, is attained.
5. Replacement position operation: The replacement position operation utilizes both the additional position and delete position operations to optimize the N_T positions within the updated optimal measurement position set U_O, as determined in the preceding step.
6. Replace position operation: The N_T positions within the updated optimal measurement position set U_O from the preceding step are optimized using both additional position and delete position operations.
7. Multi-source parallel search: Steps 3–6 are concurrently executed to compute the K optimal measurement positions within a single iteration set U_O corresponding to the observability index value, with the set yielding the highest value being recorded.
8. Global optimal solution: The algorithm attains its global optimal solution through iterative execution of steps 2–6.

Upon selecting the optimal stroke, the chosen measurement position set is determined by the optimal indicator value. Subsequently, each position within the current optimal pose set undergoes sequential replacement, resulting in the selection of optimal measurement point positions.

3.3 Measurement and identification strategy

In accordance with the chosen optimal quantity of measurement positions, distinct error measurement paths can be formulated using a comprehensive geometric error model. Table 3 enumerates the selected measurement points for the motion axis measurement stroke, guided by the inverse distance of observability analysis (IDOA).

In the measurement of *X*-axis motion, the coordinates of the smallest and largest measurement points are selected, mirroring the approach taken for the *Y*- and *Z*-axes. The measurement path is illustrated in Fig. 4.

To enhance measurement efficiency, the research group employed a sensorless measurement method developed by them to gauge positioning errors [44], while angle and straightness measurements were conducted using laser interferometry. The measurement and identification process is illustrated in Fig. 5. The fundamental concept of their measurement and identification strategy involves utilizing

Table 3 The selected measurement points based on improved D-optimal

Motion axis	Key measurement points
X-axis	P1(−253.6, −204.1, −152.5); P2(53.1, −204.1, 52.8); P3(−250.6, −195.4, −152.5); P4(100.1, −34.7, 60.5); P5(92.4, 149.7, −152.5)
Y-axis	P6(−253.6, −204.1, −152.5); P7(−100.7, −90.6, 0); P8(−50.4, −82.2, 100); P9(90.6, 147.5, 58.3)
Z-axis	P10(−253.6, −204.1, −152.5); P11(98.5, −204.7, 150.9); P12(−253.2, 201.4, 151.7)

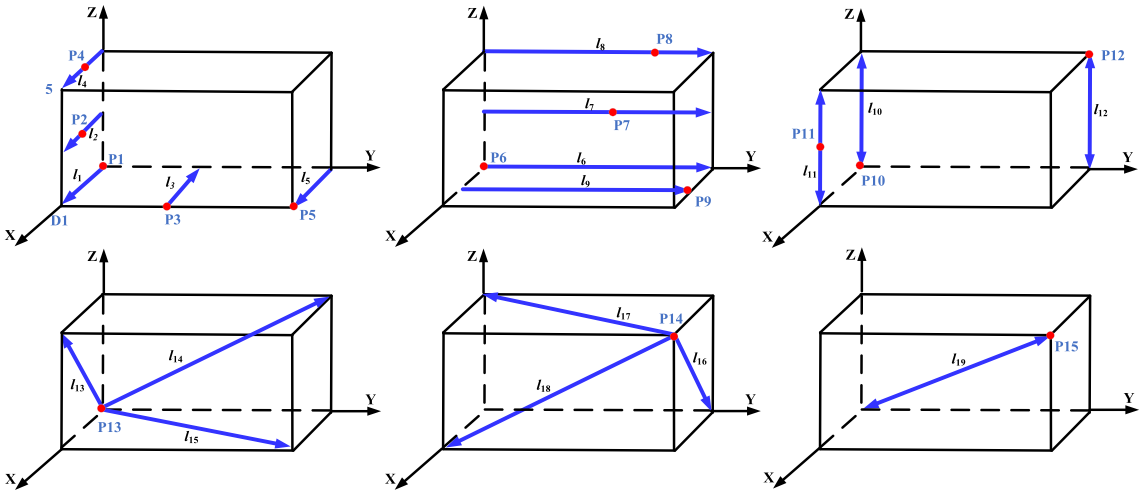

Fig. 4 Measurement path

the sensorless measurement method to assess the positioning error of the *X*-axis, alongside laser interferometry for measuring two straightness errors, two angle errors, and roll error.

For the *Y*-axis, positioning errors are measured using the sensorless measurement method, while straightness errors in the Z-direction and two angle errors (excluding rolling) are measured with the laser interferometry.

The positioning errors of the *Z*-axis are measured using the sensorless measurement method, and the two roll angle errors are measured with laser interferometry. Finally, positioning errors are measured on the face diagonal and body, along with the rolling angle and three straightness errors, including squareness error, which will be identified. For the *X*-axis, the positions of the measurement lines are all parallel to the *X*-axis. The starting point for measuring the position error (E_{XX}) is P1. The starting point for measuring the angle error (E_{BX}) along the *Y*-axis is P2, and the starting point for measuring the angle error (E_{CX}) along the *Z*-axis is P3. P4 is the starting point for measuring the straightness error (E_{YX}) in the Y-direction, and the starting point for measuring the straightness error (E_{ZX}) along the Z-direction is P5.

The positioning error is identified based on two non-rolling errors, and the coordinates of the starting point of the measurement line are determined using the sensorless measurement method:

$$E_{\mathrm{XX}} = \Delta x_1(x) + E_{CX} y_1 - E_{BX} z_1 \tag{19}$$

For measurement of the moving straightness interferometer, when both z_4 and y_5 are 0, then straightness can be identified with the measured straightness error, two non-rolling errors, and the coordinates of the starting point of the measurement line:

$$\begin{cases} \mathrm{E_{YX}} = \Delta x_4(x) - E_{CX} x_4 \\ \mathrm{E_{ZX}} = \Delta x_5(x) - E_{BX} x_4 \end{cases} \tag{20}$$

The actual straightness of the reflector's motion can be identified using the measured straightness and two non-rolling errors:

$$\begin{cases} E_{YX} = \Delta y_4(x) - E_{CX}\left(x_4 - x - L\right) \\ E_{ZX} = \Delta y_5(x) - E_{BX}\left(x_5 - x - L\right) \end{cases} \tag{21}$$

For the *Y*-axis, the positions of the measurement lines are all parallel to the *Y*-axis. The starting point for the positioning error E_{YY} is designated as P6. Additionally, the measurement starting points for angle errors are as follows: E_{AZ} at P7 and E_{CY} at P8. The starting point for assessing straightness error, E_{ZY}, is identified as P9. Concerning the *Z*-axis, the positions of the measurement lines align parallel to it. The measurement starting point for the positioning error E_{ZZ} is assigned to P10. Furthermore, the starting points for angle errors are specified as follows: E_{AZ} around the *X*-axis begins at P11, while E_{BZ} around the *Y*-axis commences at P12.

The positioning error of the three diagonal lines is measured in the XZ, XY, and YZ planes. Specifically, the positioning error of diagonal line l_{13} in the XZ plane is assessed from point P13.

In the XZ plane, where motion along the *Y*-axis is absent, the formula is simplified as follows:

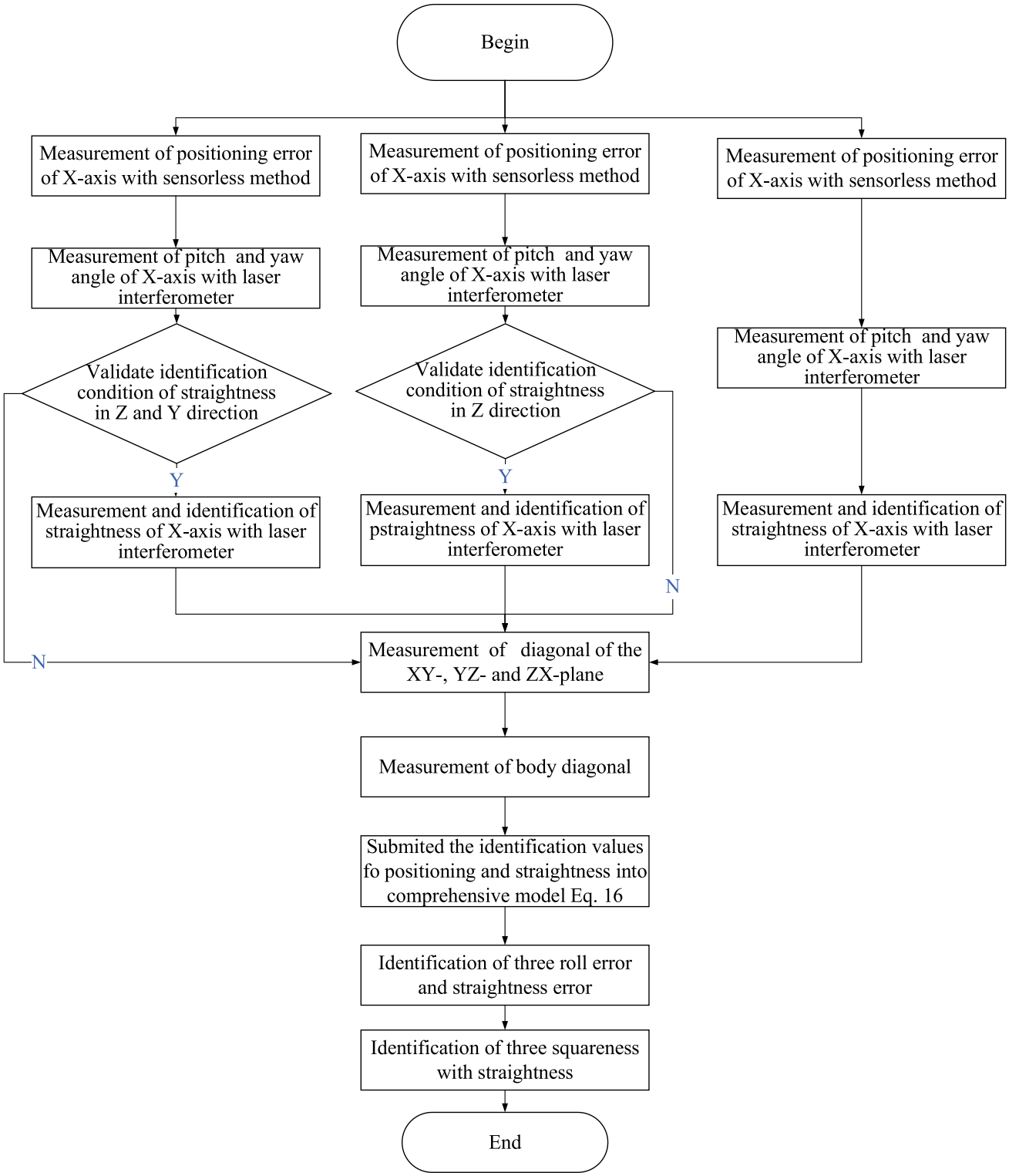

Fig. 5 Measurement and identification process

$$\begin{cases} \Delta x_{13}(x) = E_{XX} - E_{XZ} + zE_{BX} - y_{t13}\left(E_{\mathrm{CX}} - E_{\mathrm{CZ}}\right) + z_{t13}\left(E_{BX} - E_{BZ}\right) \\ \Delta z_{13}(x) = -E_{ZX} - E_{ZZ} - xE_{BX} - x_{t13}\left(E_{BX} - E_{BZ}\right) + y_{t13}\left(E_{AX} - E_{AZ}\right) \\ \Delta x_{14}(x) = E_{XX} - E_{XZ} + zE_{BX} - y_{t14}\left(E_{\mathrm{CX}} - E_{\mathrm{CZ}}\right) + z_{t14}\left(E_{BX} - E_{BZ}\right) \\ \Delta z_{14}(x) = -E_{ZX} - E_{ZZ} - xE_{BX} - x_{t14}\left(E_{BX} - E_{BZ}\right) + y_{t14}\left(E_{AX} - E_{AZ}\right) \end{cases} \tag{22}$$

Based on the error model and planar geometric relationships,

$$\begin{cases} \Delta L_{13} = \Delta x_{13}\frac{L_x}{L_{xz}} + \Delta \mathrm{z}_{13}\frac{L_z}{L_{xz}} \\ \Delta L_{14} = \Delta x_{14}\frac{L_x}{L_{xz}} + \Delta \mathrm{z}_{14}\frac{L_z}{L_{xz}} \end{cases} \tag{23}$$

The measurement starting point of positioning error of the diagonal line ΔL_{14} in the XY plane is from P14. The measurement starting point of positioning error of the diagonal line ΔL_{15} in the YZ plane is from P15.

For the XY plane, where there is no motion on the *Z*-axis, the error formula is simplified as follows:

$$\begin{cases} \Delta x_{15} = \mathrm{E_{XX}} + \mathrm{E_{XY}} + y\left(E_{CX} + E_{CY}\right) - y_{t15}\left(E_{CX} + E_{CY}\right) + z_{t15}\left(E_{BX} + E_{BY}\right) \\ \Delta y_{15} = E_{YX} + E_{YY} - xE_{CX} + x_{t15}\left(E_{\mathrm{CX}} + E_{CY}\right) - z_{t15}\left(E_{AX} + E_{AY}\right) \\ \Delta x_{16} = \mathrm{E_{XX}} + \mathrm{E_{XY}} + y\left(E_{CX} + E_{CY}\right) - y_{t16}\left(E_{CX} + E_{CY}\right) + z_{t16}\left(E_{BX} + E_{BY}\right) \\ \Delta y_{16} = E_{YX} + E_{YY} - xE_{CX} + x_{t16}\left(E_{\mathrm{CX}} + E_{CY}\right) - z_{t16}\left(E_{AX} + E_{AY}\right) \end{cases} \tag{24}$$

According to the error formula, it can be simplified as follows:

$$\begin{cases} \Delta L_{15} = \Delta x_{15}\frac{L_x}{L_{xy}} + \Delta y_{15}\frac{L_y}{L_{xy}} \\ \Delta L_{16} = \Delta x_{16}\frac{L_x}{L_{xy}} + \Delta y_{16}\frac{L_y}{L_{xy}} \end{cases} \tag{25}$$

The measurement starting point of positioning error of the diagonal line ΔL_{15} in the YZ plane is from P15. For the YZ plane, where there is no motion on the *X*-axis, the error formula is simplified as follows:

$$\begin{cases} \Delta y_{15} = E_{YY} - E_{YX} - zE_{AY} - x_{t15}\left(E_{CY} - E_{CZ}\right) - z_{t15}\left(E_{AY} - E_{AZ}\right) \\ \Delta z_{15} = -E_{ZY} + E_{ZZ} - x_{t15}\left(E_{BY} - E_{BZ}\right) + z_{t15}\left(E_{AY} - E_{AZ}\right) \\ \Delta y_{16} = E_{YY} - E_{YX} - zE_{AY} - x_{t16}\left(E_{CY} - E_{CZ}\right) - z_{t16}\left(E_{AY} - E_{AZ}\right) \\ \Delta z_{16} = -E_{ZY} + E_{ZZ} - x_{t16}\left(E_{BY} - E_{BZ}\right) + z_{t16}\left(E_{AY} - E_{AZ}\right) \end{cases} \tag{26}$$

Based on the error model and planar geometric relationships,

$$\begin{cases} \Delta L_{15} = \Delta x_{15}\frac{L_x}{L_{xy}} + \Delta y_{15}\frac{L_y}{L_{xy}} \\ \Delta L_{16} = \Delta x_{16}\frac{L_x}{L_{xy}} + \Delta y_{16}\frac{L_y}{L_{xy}} \end{cases} \tag{27}$$

The measurement starting point of positioning errors of the XYZ diagonal ΔL_{16} are measured from P16; the angles between the diagonal and the *X*-, *Y*-, and *Z*-axes are α, β, and γ, by incorporating each measurement position into the error model; according to the positioning error of the diagonal, it can be inferred that

$$\Delta L_{17} = \Delta x_{17}cos\boldsymbol{\alpha} + \Delta \mathrm{y}_{17}cos\boldsymbol{\beta} + \Delta z_{17}cos\boldsymbol{\gamma} \tag{28}$$

With the measurement path and identification equation, all straightness errors and roll angle errors can be obtained using the least squares method.

4 Parametric modeling of error terms and uncertainty optimization

4.1 Parametric modeling of geometric error terms

The established comprehensive error model of machine tools comprises individual errors of motion axes, with each axis represented as discrete points. Therefore, it is imperative to develop modeling methods to parameterize the measured individual error data.

Analysis of the error data acquired from measurements reveals that positioning error and partial straightness error exhibit relatively minor fluctuations, allowing for effective modeling using low-order orthogonal polynomials. In contrast, although angular error values are relatively small, they demonstrate significant fluctuations, often manifesting in marked periodic oscillations. Consequently, a parametric model is proposed that utilizes exponential cosine fitting, amalgamating the data characteristics of these three geometric errors. The model is defined as follows:

$$y = a \cdot e^{b \cdot i} \cdot cos(c \cdot i) + d \cdot i + e(i = x, y, z) \tag{29}$$

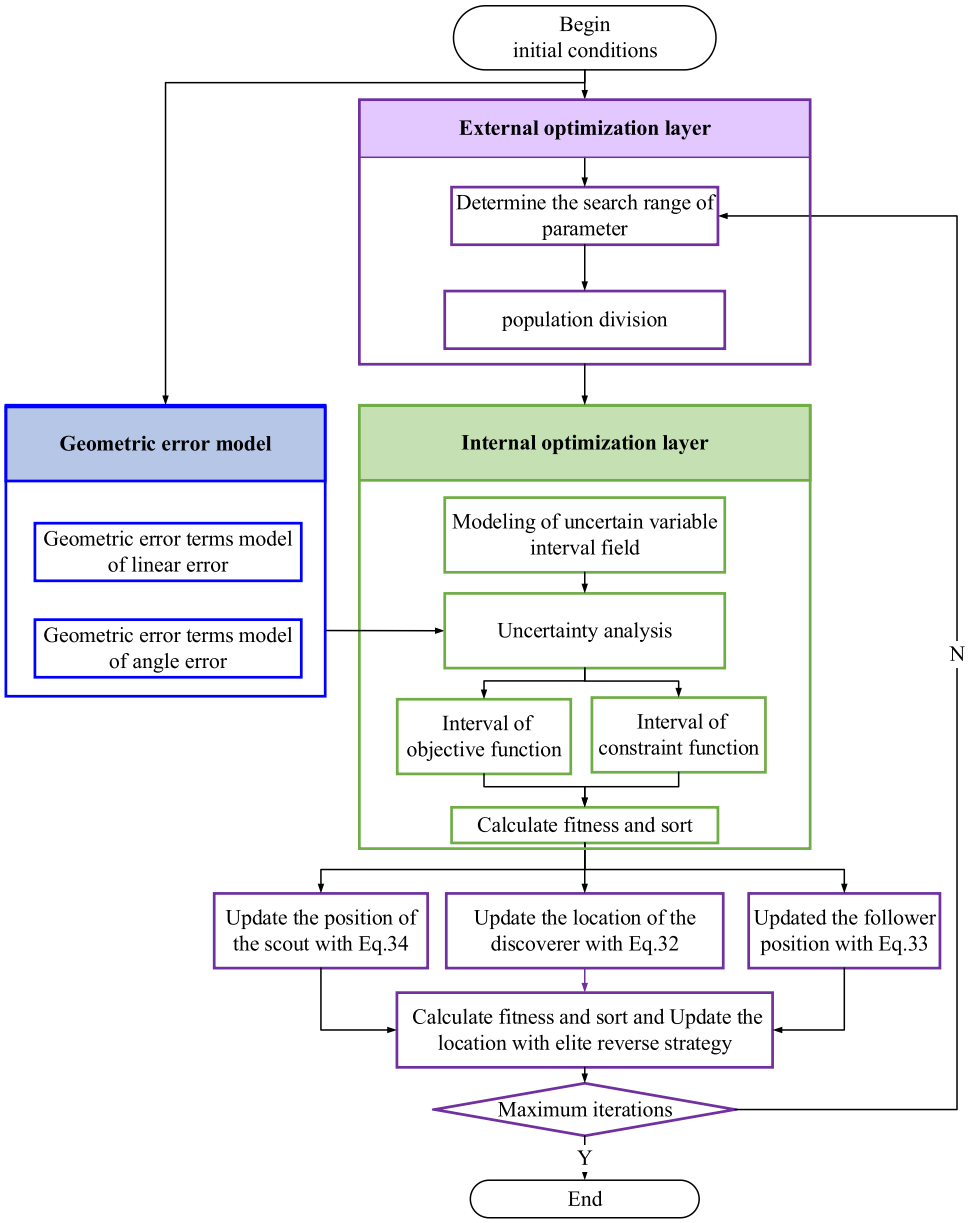

Fig. 6 Optimization process of fitting optimization

where x represents the position of the guide rail; y represents the error value here; and a, b, c, d, and e are undetermined parameters.

In the optimization framework, the optimization process is bifurcated into two layers, comprising inlay optimization. The ISSA is employed to optimize the parametric model of exponential cosine fitting in the outer layer. Utilizing the interval method, the range of uncertain objective functions and constraint functions is calculated. In the inner layer, the fitness of the design variables is determined by resolving the transformed objective function. The sequential process unfolds in Fig. 6.

1. The initial optimization conditions can be determined based on the optimization problem, which includes variables, uncertain parameters, and parameter space.
2. The model for the cosine-exponential product geometric error term is constructed according to the optimization objective and uncertainty parameters.
3. The optimization process involves a two-layer nested loop.
4. The ISSA is employed to generate the initial population of variables for the error model optimization.
5. From the current population, a set of values for the variables is selected and subjected to inner uncertainty analysis using the interval to model uncertainty.
6. The current uncertainty parameter variables are incorporated based on the constructed geometric error model, and the intervals for the geometric error term and uncertainty constraint function are calculated.

7. The fitness of the current design variables is evaluated using the fitness function.
8. Steps 5–7 are iterated until the fitness of all individuals in the current population is computed and individual fitness is assessed.
9. When the convergence criteria are satisfied, the optimization concludes. The current population is then output as the optimization result. If not, the process returns to step 4.

Due to its incorporation of low-order polynomials in positioning and straightness errors, alongside angle error fluctuations, this model embodies typical nonlinear characteristics. However, solving its undetermined parameters using numerical methods presents significant computational complexity, making optimal parameter identification challenging. Hence, intelligent optimization algorithms, such as the SSA, are considered, which is inspired by sparrows' foraging and anti-predatory behavior and categorizes individuals as discoverers and followers, with additional reconnaissance and warning mechanisms. The operation process is as follows:

Establishing the parameter search range In the exponential cosine fitting model, a is the exponential cosine monomial amplification coefficient, which determined by the maximum and minimum values of each geometric error term in actual identification; b represents the fluctuation coefficient of the exponential function and within $[-1, 1]$; c represents the expansion factor of the cosine curve and within $[0, 2]$; d represents the degree of divergence of the error fitting curve, which determined by the geometric error value at the current command position, the minimum and maximum geometric errors of the motion axis at the current position and within $[-1, 1]$; e represents the error value when the motion axis is at the initial position, which can be determined based on the maximum and minimum values of the input error data, as well as the adjustment coefficient k, and within $[k_{ymin}, k_{ymax}]$.

Population initialization The sparrow population matrix is shown in Eq. 30:

$$X = \begin{pmatrix} x_1^1 & x_1^2 & \cdots & x_1^d \\ x_2^1 & x_2^2 & \cdots & x_2^d \\ \cdots & \cdots & \cdots & \cdots \\ x_n^1 & x_n^2 & \cdots & x_n^d \end{pmatrix} \tag{30}$$

where x represents the sparrow population, d represents the spatial dimension, and n represents the number of sparrows.

Calculate fitness values and sort The objective function value is determined by the sum of residual squares, as depicted in Eq. 31. A smaller value indicates closer proximity of the sparrow to the food.

$$fit = \sum_{j=1}^{m} \left(y_i - y\right)^2 \tag{31}$$

A smaller fitness function value signifies a smaller deviation between the predicted and actual values, indicating the sparrow's position is closer to the target value. This suggests that the parameter set is more likely to be the optimal solution.

Update the location of the discoverer

$$x_{i,d}^{t+1} = \begin{cases} x_{i,d}^t \cdot e^{\left(\frac{-i}{\alpha \cdot \mathrm{iter}_{max}}\right)}, R_2 < ST \\ x_{i,d}^t + Q, R_2 > ST \end{cases} \tag{32}$$

where $x_{i,d}^t$ represents the d-th dimensional position of the i-th individual in the t-th generation of the sparrow population; α is a uniform random number between (0, 1); $iter_{max}$ is the maximum number of iterations; Q is the standard normal distribution random number; R_2 represents the warning value, which is a uniform random number between [0, 1]; and ST represents the safety value, which is within the range of [0.5, 1].

When ($R_2 > ST$), the discoverer randomly moves to the current position following a normal distribution. Conversely, when ($R_2 < ST$), the discoverer moves randomly in a monotonically decreasing exponential manner. With a fixed maximum number of iterations, the search range decreases gradually as the value increases, a reduction in the sparrow's dimensionality, with the minimum value converging towards zero.

Update the follower position

$$x_{t,d}^{t+1} = \begin{cases} Q \cdot e^{\left(\frac{xw_{i,d}^i - x_{i,d}^t}{i^2}\right)}, i > n/2 \\ xb_{i,d}^t + \frac{1}{d}\sum_{d=1}^{d}(rand\{-1,1\} \cdot (\left|xb_{i,d}^t - x_{i,d}^t\right|)), i \le n/2 \end{cases} \tag{33}$$

where d represents the spatial dimension, $xw_{i,d}^t$ represents the worst position in the d-th dimension of the i-th individual in the t-th generation of the sparrow population, $xb_{i,d}^t$ represents the d-th optimal position of the i-th individual in the t-th generation of the sparrow population, and n represents the number of sparrows. When $i > n/2$, the follower's position is determined by multiplying a standard normal distribution random number by an exponential function with e. This value adheres to the standard normal distribution and tends to converge towards zero. The follower's position acquisition process can be illustrated as follows: when $i \le n/2$, it involves randomly searching for a position near the current optimal sparrow position. As i increases,

the variance of each dimensional distance from the optimal position decreases, leading to convergence towards the optimal position. Moreover, the variance of each dimensional distance from the optimal position becomes similar to that of other positions.

Update the position of the scout

$$x_{i,d}^{t+1} = \begin{cases} x_{i,d}^{t} + \beta \cdot (x_{i,d}^{t} - xb_{i,d}^{t}), f_i \neq f_g \\ x_{i,d}^{t} + \beta \cdot (xw_{i,d}^{t} - xb_{i,d}^{t}), f_i = f_g \end{cases} \tag{34}$$

The sparrow algorithm employs two methods for updating its position: jumping to the current optimal position and approaching the origin. However, the update strategy of the sparrow algorithm may encounter challenges leading to local optima. To enhance its capability to find the global optimal solution, three improvements have been introduced to the sparrow algorithm:

1. The adjustment to the finder positions is executed by eliminating operations that draw them closer to the origin, prioritizing a leap towards the current optimal position.

$$x_{i,d}^{t+1} = \begin{cases} x_{i,d}^{t} \cdot (1 + Q), R_2 < ST \\ x_{i,d}^{t} + Q, R_2 > ST \end{cases} \tag{35}$$

2. The update strategy for follower positions entails a random movement towards the discoverer position. The modification to the formula is delineated in Eq. 36:

$$x_{i,d}^{t+1} = xb_{i,d}^{t} + \frac{1}{d}\sum_{d=1}^{d}(rand\{-1,1\} \cdot (\left|xb_{i,d}^{t} - x_{i,d}^{t}\right|)) \tag{36}$$

3. Elite reverse strategy:

$x_{i,d}^{t} = (x_{i,1}^{t}, x_{i,2}^{t}..., x_{i,d}^{t})$ Is the solution generated by the t-th iteration of the sparrow algorithm; then, the inverse solution is $x_{i,d}^{t*}$. When $fit(x_{i,d}^{t}) \geq fit(x_{i,d}^{t*})$, $x_{i,d}^{t}$ is the elite individual of the t-th iteration and is denoted as $Q_{i,d}^{t}$. The reverse solution $Q_{i,d}^{t*}$ can be expressed as $Q_{i,d}^{t*} = K \cdot (\alpha_d + \beta_d) - Q_{i,d}^{t}$, K is the dynamic coefficient with in $[0, 1]$,$Q_{i,d}^{t} \in [\alpha_d, \beta_d]$; $a_d = min\left(Q_{i,d}^{t}\right)$;$\beta_d = max(Q_{i,d}^{t})$ is a dynamic boundary.

A more efficient search approach can be achieved through the implementation of a dynamic boundary algorithm, which adjusts according to the optimal solution during the search process, particularly in scenarios where the search space is constrained. Utilizing SSA to solve geometric error model parameters represents a typical single-objective function optimization problem.

4.2 Optimization method of error term based on interval uncertainty

In traditional deterministic optimization problems, all parameters within the optimization model are designated as constant values. The objective function and constraints can be computed for a given variable point. However, when dealing with geometric error terms, characterized by uncertainty, both the objective function and constraint function become uncertain, transforming the deterministic optimization problem into an uncertain one. The interval uncertainty optimization method is employed to model and optimize error parameters. The general interval uncertainty optimization model can be expressed as

$$\begin{cases} \min\limits_{X} f(X, U) \\ \text{s.t.} g_i(X, U) \leq b_i^{\mathrm{I}} = \left[b_i^{\mathrm{L}}, b_i^{\mathrm{R}}\right], i = 1,2, \cdots l \\ U_i \in U_i^{\mathrm{I}} = \left[U_i^{\mathrm{L}}, U_i^{\mathrm{R}}\right], i = 1,2, \cdots q \end{cases} \tag{37}$$

where X is an n-dimensional design variable that geometric error term with a value range of Ω_{n}, U is the q dimensional interval uncertainty variable, U_{L} is the lower boundary, and U_{R} is the upper boundary. f and g are continuous functions of X and U, respectively, and b_{Ii} is the i-th uncertainty constraint.

For the objective function $f(X, U)$, the interval uncertainty can be described as

$$f(X, U) \in f^{\mathrm{I}}(X) = \left[f^{\mathrm{L}}(X), f^{\mathrm{R}}(X)\right] \tag{38}$$

The upper and lower bounds of the objective function can be analyzed by interval analysis methods.

$$\begin{cases} f^{\mathrm{L}}(X) = \min\limits_{U} f(X, U) \\ f^{\mathrm{R}}(X) = \max\limits_{U} f(X, U) \end{cases} \tag{39}$$

The uncertain objective function can be converted into a deterministic optimization objective function by handling the interval midpoint and interval radius. The optimal variable can then be identified by assessing the deterministic objective function. The weighted linear combination of the uncertain objective function is depicted in Eq. (41):

$$\begin{aligned} \min f(X) &= (1 - \beta)(f^{c}(X) + \xi)/\phi + \beta(f^{w}(X) + \xi)/\varphi \\ f^{c}(X) &= \tfrac{1}{2}\left(f^{\mathrm{R}}(X) + f^{\mathrm{L}}(X)\right) \\ f^{w}(X) &= \tfrac{1}{2}\left(f^{\mathrm{R}}(X) - f^{\mathrm{L}}(X)\right) \end{aligned} \tag{40}$$

where $0 \leq \beta \leq 1$ is a multi-objective weight coefficient. $f^{c}(X)$ and $f^{w}(X)$ are non-negative compensation coefficients. ϕ and ψ are normalized factors as follows:

$$\phi = \min_{X}(f^{c}(X) + \xi), \varphi = \min_{X}(f^{w}(X) + \xi) \tag{41}$$

The interval possibility method is employed to address the uncertainties associated with both the objective function and constraints of variables exhibiting interval uncertainty. This method presupposes that the two intervals in question are modeled as random variables following a uniform distribution. Six potential positional relationships exist for the intervals denoted as A^I and B^I, reflecting the various ways in which these intervals can intersect or relate to each other. The corresponding possibility degree is expressed in Eq. (6):

$$P\left(A^I \le B^I\right) = \begin{cases} 0 & B^R \le A^L \\ \frac{B^R - A^L}{2\left(A^R - A^L\right)} \frac{B^R - A^L}{B^R - B^L} & B^L \le A^L \le B^R < A^R \\ \frac{B^R - A^L}{A^R - A^L} + \frac{B^R - B^L}{2\left(A^R - A^L\right)} & A^L < B^L < B^R \le A^R \\ \frac{B^R - A^L}{A^R - A^L} + \frac{A^R - B^L}{A^R - A^L} \frac{B^R - A^R}{B^R - B^L} + \frac{A^R - B^L}{2\left(A^R - A^L\right)} \frac{A^R - B^L}{B^R - B^L} & A^L < B^L < A^R < A^R \\ \frac{B^R - A^R}{B^R - B^L} + \frac{A^R - A^L}{2\left(B^R - B^L\right)} & B^L \le A^L < A^R < B^R \\ 1 & A^R \le B^L \end{cases} \tag{42}$$

The uncertainty constraint function represented by Eq. 42 can be transformed into the following deterministic inequality constraint:

$$P\left(g_i^{\mathrm{I}}(X) \le b_i^{\mathrm{I}}\right) \ge \lambda_i \tag{43}$$

where $0 \le \lambda_i \le 1$ is the given interval possibility index and $g_{Ii}(X)$ is the range interval caused by uncertainty at X of the constraint function $g_i(X,U)$, and $g_i(X,U)$ can also be solved by interval global optimization method.

The possibility $P(g_{Ii}(X) \le b_{Ii})$ of the constraint can be derived using the interval possibility model once $g_{Ii}(X)$ is obtained. Subsequently, the assigned possibility can be evaluated, leading to the transformation of the uncertainty constraint into a deterministic one through this process. Following the conversion using the linear weighted combination method and possibility model, the original uncertain optimization problem evolves into a deterministic multi-objective optimization problem. The constraint conditions can then be handled using the penalty function method, thereby transforming it into an unconstrained optimization problem:

$$\begin{cases} \min\limits_X f(X) = (1-\beta)(f^c(X) + \xi)/\phi + \beta(f^w(X) + \xi)/\varphi \\ \quad +\sigma \sum_{i=1}^{l} \left[\max\left(0, P\left(g_i^{\mathrm{I}}(X) \le b_i^{\mathrm{I}}\right) - \lambda_i\right)\right]^2 \\ X \in \Omega^n \end{cases} \tag{44}$$

where σ is the penalty factor.

Mean deviation e, root mean square error RMSE, and goodness of fit R^2 are commonly utilized to assess and compare the efficacy of different models in fitting. However, these indicators exhibit three limitations. Firstly, the impact of the discreteness in geometric error data on prediction stability is neglected.

The circular trajectory before and after compensation is shown in Fig. 16.

It can be seen from Fig. 16 that a notable deviation between the circular trajectory before compensation and the standard circular trajectory, with a substantial improvement observed after compensation. The circular trajectory post-compensation aligns closely with the standard circular

Secondly, when evaluation parameters of distinct models lack significance, the distribution of deviations between the predicted and actual values cannot be directly reflected. Thirdly, evaluation parameters of modeling have not been employed for optimization to enhance fitting effectiveness. As a result, addressing model uncertainty enhances the geometric error model's fitting, which may initially be suboptimal.

Assuming (λ_i, φ_i) represents the position and identification error values of the motion axis at the i-th measurement point and $(\lambda_i, '_i)$ signifies the position and prediction error values of the motion axis at the i-th measurement point, the sum of uncertainties for all measurement points can be derived using the Bessel formula in the uncertainty principle, and the sum of uncertainties for all measurement points can be obtained as

$$\vartheta = \frac{\sqrt{\sum_{i=1}^{N} \left((\varphi_i - \varphi'_i) - \frac{1}{N}\sum_{i=1}^{N}(\varphi_i - \varphi'_i)\right)}}{N-1} \tag{45}$$

where N is the total number of measurement points and σ is the sum of the uncertainties of all measurement points. e is the average deviation value of the fitted model, as shown in Eq. 46.

$$e = \frac{1}{N}\sum_{i=1}^{N}(\varphi_i - \varphi'_i) \tag{46}$$

The uncertainty of the fitting model can be calculated with Eq. 47:

$$f(\varphi\prime|e,\vartheta) = \frac{1}{\sqrt{2\pi}\sigma} e^{\left\{-\frac{[x-e]^2}{2\sigma^2}\right\}} \tag{47}$$

A larger deviation between the predicted value and the true value corresponds to poorer predictive performance and signifies higher uncertainty within the model.

5 Case study

This experiment utilizes the VDL-600A three-axis vertical machining center, equipped with the FANUC 0i system. Each of the three motion axes is fitted with high-precision ball screw pairs, guaranteeing both positioning accuracy and repeated positioning accuracy of the machining center. Geometric error measurements are performed by carefully selecting optimal measurement times and determining the measurement stroke based on modified D-optimal criteria.

5.1 Parametric modeling of geometric error terms

Based on the measurements and identification results of geometric errors, parametric modeling of geometric errors is conducted following the modeling flow outlined in Sect. 3. Taking the modeling of the exponential cosine for the positioning error on the *X*-axis as an example, the population size of the ISSA is set to 50, with 50 iterations. The proportions of investigators, discoverers, and followers are set to 0.6, 0.8, and 0.3 respectively, with these proportional parameters remaining constant throughout the iterations. The iteration curve of the ISSA is depicted in Fig. 7.

It can be seen from Fig. 7 that the enhanced sparrow search algorithm (SSA) surpasses the standard SSA in both search efficiency and accuracy. The six geometric error data points for the *X*-axis, identified and fitted using the measurement method outlined in Sect. 3, undergo post-processing with the ISSA. The uncertainty of the fitting curve is calculated using Eqs. 36 and 37, as presented in Table 4.

It can be inferred from Table 4 that the uncertainty σ and average deviation e of the exponential cosine fitting model for the geometric error terms E_{ZX} and E_{CX} are larger than those

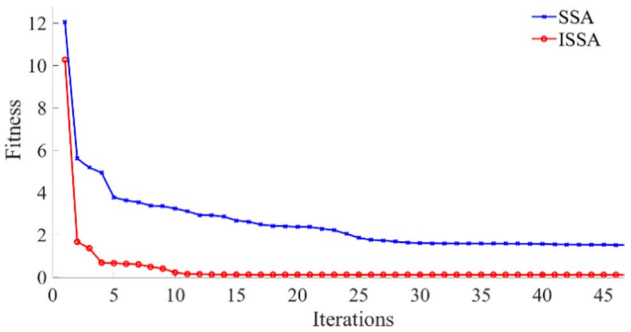

Fig. 7 Algorithm convergence curve

Table 4 Comparison of uncertainty parameter of *X*-axis geometric error model

Error terms	ECFM		OPFM	
	σ	e	σ'	e'
E_{XX}/(μm)	0.21	0.18	0.41	0.31
E_{YX}/(μm)	0.03	0.02	0.09	0.08
E_{ZX}/(μm)	0.58	0.47	0.26	0.21
E_{AX}/(μm/mm)	1.57×10^{-4}	1.32×10^{-4}	5.98×10^{-5}	4.25×10^{-5}
E_{CX}/(μm/mm)	1.00×10^{-4}	7.61×10^{-5}	1.40×10^{-4}	1.12×10^{-4}
E_{BX}/(μm/mm)	3.10×10^{-4}	2.50×10^{-4}	3.51×10^{-4}	2.84×10^{-4}
E_{XY}/(μm)	0.06	0.05	1.26	1.07
E_{YY}/(μm)	0.20	0.14	0.42	0.32
E_{ZY}/(μm)	0.01	0.01	0.03	0.03
E_{CY}/(μm/mm)	3.40×10^{-5}	3.39×10^{-5}	5.54×10^{-5}	5.25×10^{-5}
E_{BY}/(μm/mm)	3.14×10^{-5}	2.82×10^{-5}	1.67×10^{-4}	1.50×10^{-4}
E_{AY}/(μm/mm)	1.21×10^{-4}	1.04×10^{-4}	2.76×10^{-4}	2.02×10^{-4}
E_{XZ}/(μm)	0.02	0.02	0.03	0.02
E_{YZ}/(μm)	0.05	0.04	1.39	0.08
E_{ZZ}/(μm)	0.83	0.66	1.12	0.90
E_{BZ}/(μm/mm)	5.99×10^{-5}	4.56×10^{-5}	7.38×10^{-5}	5.64×10^{-5}
E_{AZ}/(μm/mm)	3.84×10^{-5}	3.37×10^{-5}	1.62×10^{-4}	1.39×10^{-4}
E_{CZ}/(μm/mm)	1.84×10^{-4}	1.50×10^{-4}	3.08×10^{-4}	2.26×10^{-4}

of the orthogonal polynomial fitting model. It reveals that the uncertainty σ and average deviation e of the ECFM are lower compared to those of the OPFM. This observation suggests that the ECFM model offers superior error prediction accuracy compared to the OPFM model. Hence, the ECFM model proves to be more suitable for fitting and forecasting geometric errors in machine tools. It also indicates the model's fitting performance is inadequate, resulting in lower prediction accuracy compared to the orthogonal polynomial fitting model. Consequently, there is a need for further optimization of the model based on the uncertainty optimization method. Monte Carlo sampling was employed to simulate parameter ranges. The search intervals for the optimized parameters of E_{ZX} and E_{CX} are illustrated in Fig. 8a, b, respectively.

The percentage of each partition within the model parameter interval that satisfies the optimization conditions varies after optimizing the model parameter interval using nested parameter uncertainty optimization. A higher percentage within the parameter interval indicates a greater likelihood of optimal solutions. Therefore, the parameter interval with the highest percentage is selected for substitution into the ISSA. This process facilitates the modeling of error terms E_{ZX} and E_{CX}. The uncertainty of fitting the model of E_{ZX} is $\sigma=0.0043<\sigma'=0.26$, average deviation $e=0.0035<e'=0.21$. The uncertainty of fitting model of E_{CX} is $\sigma=5.35\times10^{-5}<\sigma'=5.98\times10^{-5}$, average deviation $e=3.79\times10^{-5}<e'=4.25\times10^{-5}$. The uncertainty curves of the model before and after optimization can be obtained by substituting into Eq. 38, as shown in Fig. 9.

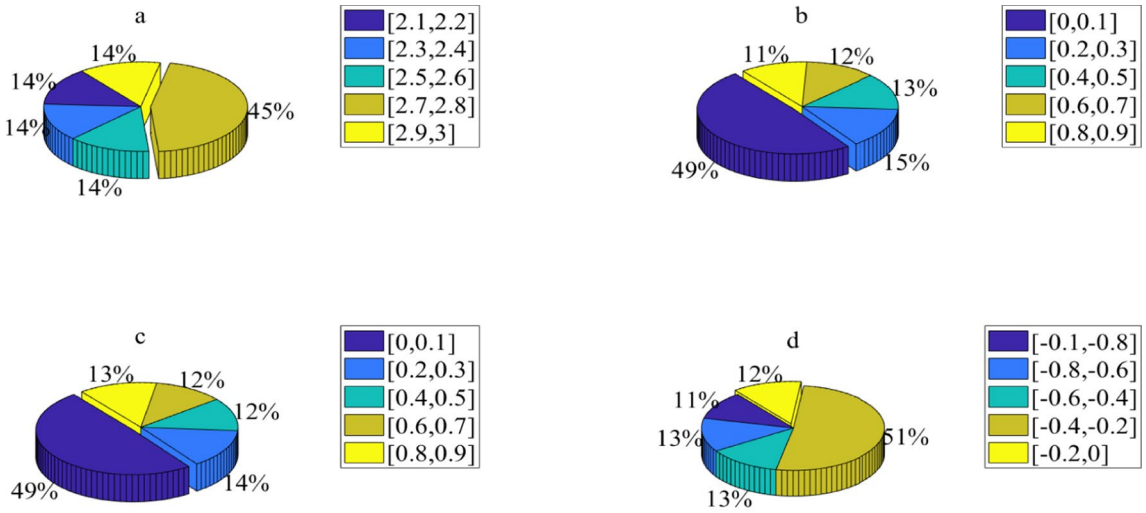

(a) search interval of straightness error E_{ZX}

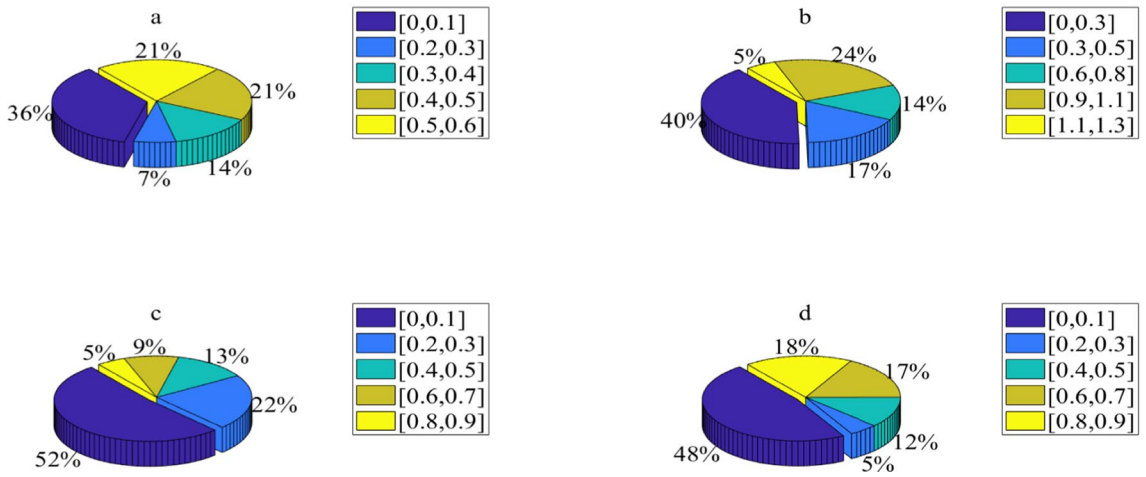

(b) Search interval of rolling error E_{CX}

Fig. 8 Search interval of the model after optimized

It can be seen from Fig. 9 that the predicted residuals of the fitting model E_{ZX} are concentrated within the range of − 0.4 to 0.4 μm. Similarly, the predicted residuals of E_{AX} are confined within the range of − 0.0002 to 0.0002 μm/mm, exhibiting a sharper curve distribution and a narrower range of predicted residuals. This suggests that a smaller deviation between the predicted and true values results in smaller uncertainty for the optimized ECFM.

By substituting the model parameter values calculated by the ISSA into the fitting model, the expression of geometric error for the *X*-axis fitting curve can be derived, which is presented in Eq. 48:

$$\begin{cases} E_{XX} = -0.2265 \cdot e^{(-0.01412 \cdot x)} \cdot cos(-0.02074 \cdot x) + 0.05106 \cdot x + 10.14 \\ E_{YX} = -0.188 \cdot e^{(-0.001582 \cdot x)} \cdot cos(0.03508 \cdot x) - 0.002988 \cdot x - 0.086 \\ E_{ZX} = 2.752 \cdot e^{(0.01701 \cdot x)} \cdot cos(0.007901 \cdot x) - 0.02435 \cdot x - 3.812 \\ E_{CX} = 0.0002559 \cdot e^{(0.002212 \cdot x)} \cdot cos(0.04339 \cdot x) - 0.000002318 \cdot x - 0.001223 \\ E_{BX} = -0.0007139 \cdot e^{(0.02505 \cdot x)} \cdot cos(0.0136 \cdot x) + 0.00002097 \cdot x + 0.002469+ \\ E_{AX} = 0.0002857 \cdot e^{(0.006122 \cdot x)} \cdot cos(0.0223 \cdot x) + 0.000004032 \cdot x - 0.00003137 \end{cases} \quad (48)$$

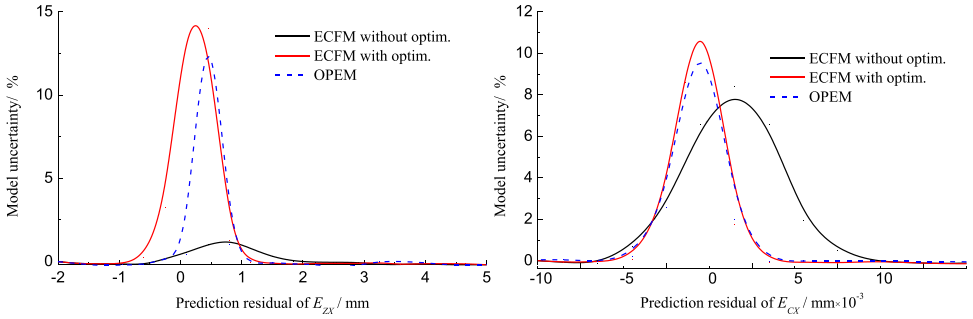

(a) Model uncertainty of E_{ZX} (b) Model uncertainty of E_{CX}

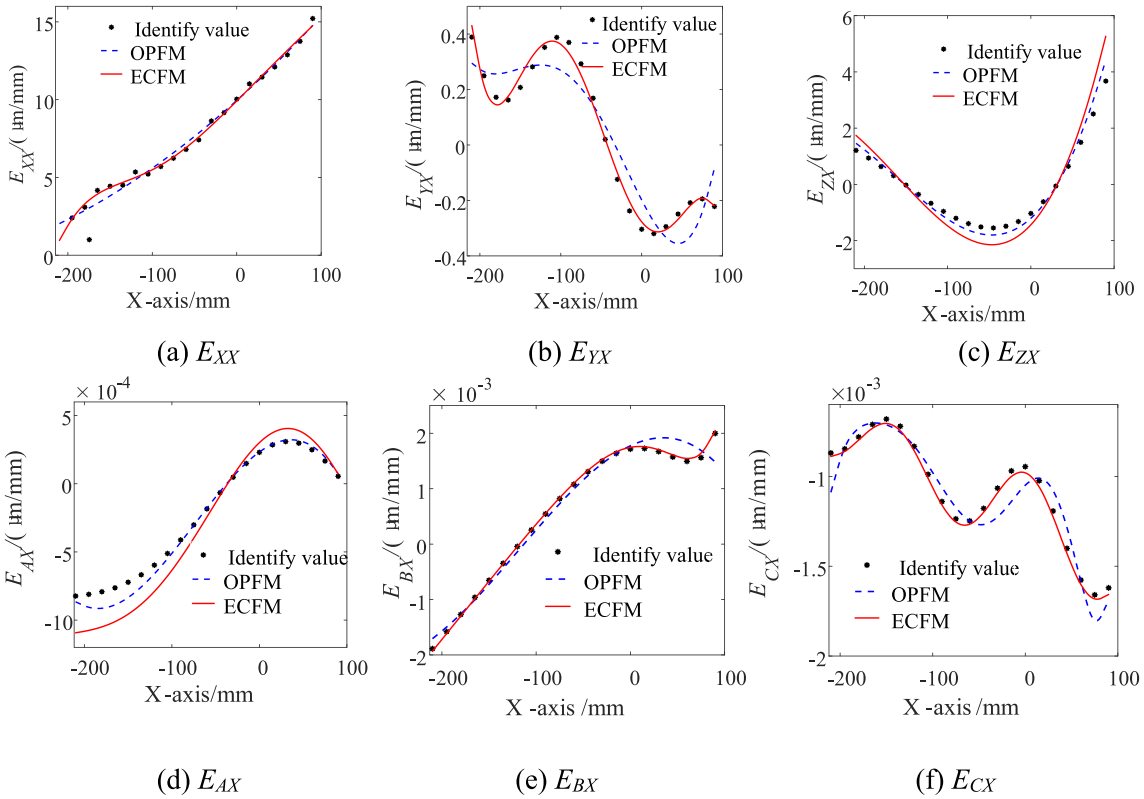

(a) E_{XX} (b) E_{YX} (c) E_{ZX}

(d) E_{AX} (e) E_{BX} (f) E_{CX}

Fig. 10 *X*-axis geometric error fitting model

The model of six geometric errors of the *Y*-axis is shown in Eq. 49.

$$\begin{cases} E_{\mathrm{YY}} = 0.5793 \cdot e^{(-0.0001423 \cdot y)} \cdot cos(0.05238 \cdot y) + 0.04008 \cdot y + 6.84 \\ E_{\mathrm{XY}} = -11.4 \cdot e^{(0.004718 \cdot y)} \cdot cos(0.004338 \cdot y) + 0.04924 \cdot y + 11.52 \\ E_{\mathrm{ZY}} = 3.013 \cdot e^{(-0.004432 \cdot y)} \cdot cos(0.05285 \cdot y) + 0.0009422 \cdot y - 0.2605 \\ E_{\mathrm{AY}} = 0.00008096 \cdot e^{(0.03595 y)} \cdot cos(0.008673 \cdot y) - 0.00003888 \cdot y - 0.003602 \\ E_{\mathrm{CY}} = 3.086 \cdot e^{(-0.004432 \cdot y)} \cdot cos(0.05282 \cdot y) + 0.0009652 \cdot y - 0.2669 \\ E_{\mathrm{BY}} = -0.0001554 \cdot e^{(-0.01796 \cdot y)} \cdot cos(0.03604 \cdot y) - 0.00000913 \cdot y + 0.001874 \end{cases} \tag{49}$$

The model of six geometric errors of the *Z*-axis is shown in Eq. 50.

$$\begin{cases} E_{ZZ} = -0.4363 \cdot e^{(-0.003412 \cdot z)} \cdot cos(0.1012 \cdot z) - 0.0984 \cdot z - 14.37 \\ E_{XZ} = -0.01715 \cdot e^{(0.02412 \cdot z)} \cdot cos(0.02514 \cdot z) - 0.003974 \cdot z - 0.2031 \\ E_{YZ} = 2.516 \cdot e^{(0.007911 \cdot z)} \cdot cos(0.007296 \cdot z) - 0.01369 \cdot z - 2.303 \\ E_{AZ} = 0.0008998 \cdot e^{(0.005862 \cdot z)} \cdot cos(0.02765 \cdot z) - 0.000001783 \cdot z + 0.0005033 \\ E_{BZ} = 0.009668 \cdot e^{(0.01052 \cdot z)} \cdot cos(0.006298 \cdot z) - 0.00007605 \cdot z - 0.01028 \\ E_{CZ} = -0.001752 \cdot e^{(-0.00104 \cdot z)} \cdot cos(0.01821 \cdot z) + 0.000007631 \cdot z + 0.0006596 \end{cases} \tag{50}$$

The parameterized model curve depicting the six geometric errors of the linear axes is illustrated in Figs. 10, 11, and 12.

Model curves of the *Z*-axis six geometric errors are shown in Fig. 12.

As can be seen from Figs. 10, 11, and 12, the sinusoidal straightness error is the most common type encountered. The error curve of three linear axes exhibits fluctuations both upwards and downwards, with slight periodicity. For positioning errors, the midsection of the motion axis bears its own weight or that of the spindle. Hence, during the design phase of machine tools, pre-bending is typically incorporated. However, due to prolonged machining, wear, and loading, the entire motion axis guide rail inevitably bends downwards. Generally, this guide rail bends downwards and results in a geometric error shape akin to linear variation.

5.2 Validity verification of compensation experiment

The experiments were performed on a VDL-600A three-axis vertical machining center using a geometric error–assisted

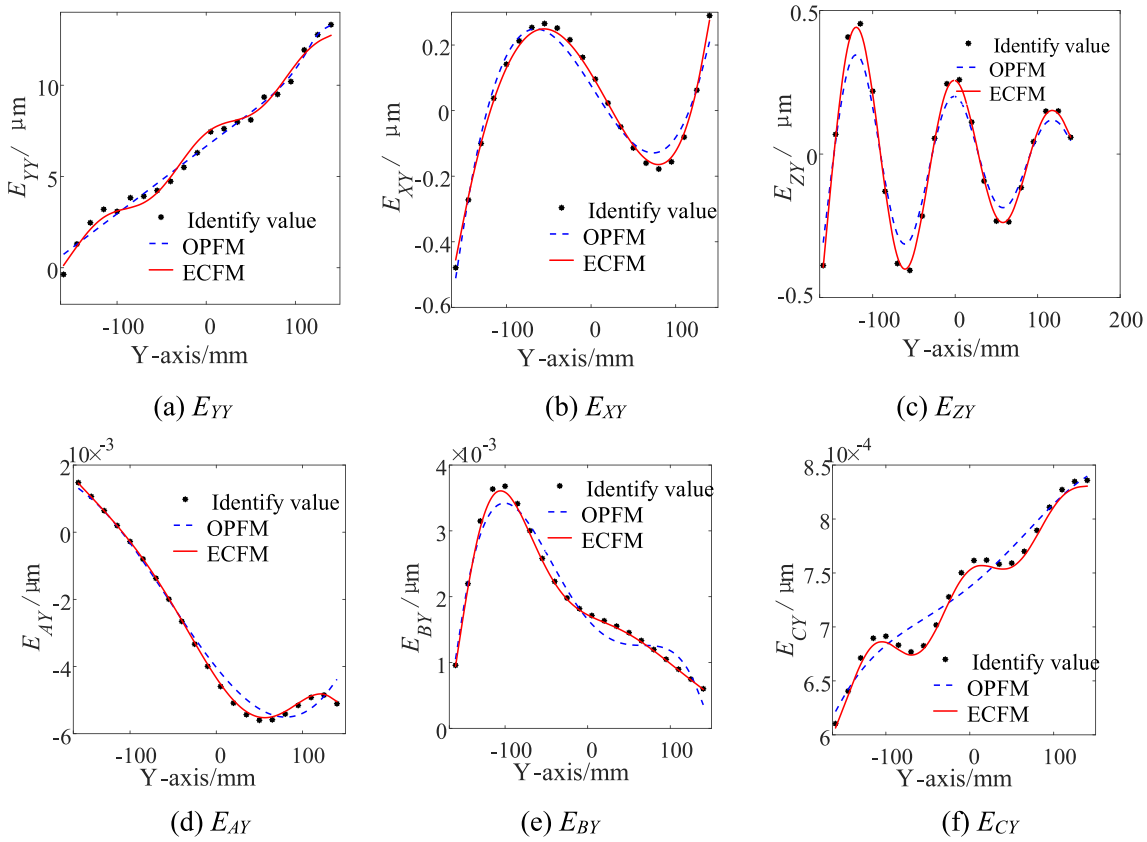

Fig. 11 Fitting cure of *Y*-axis geometric error

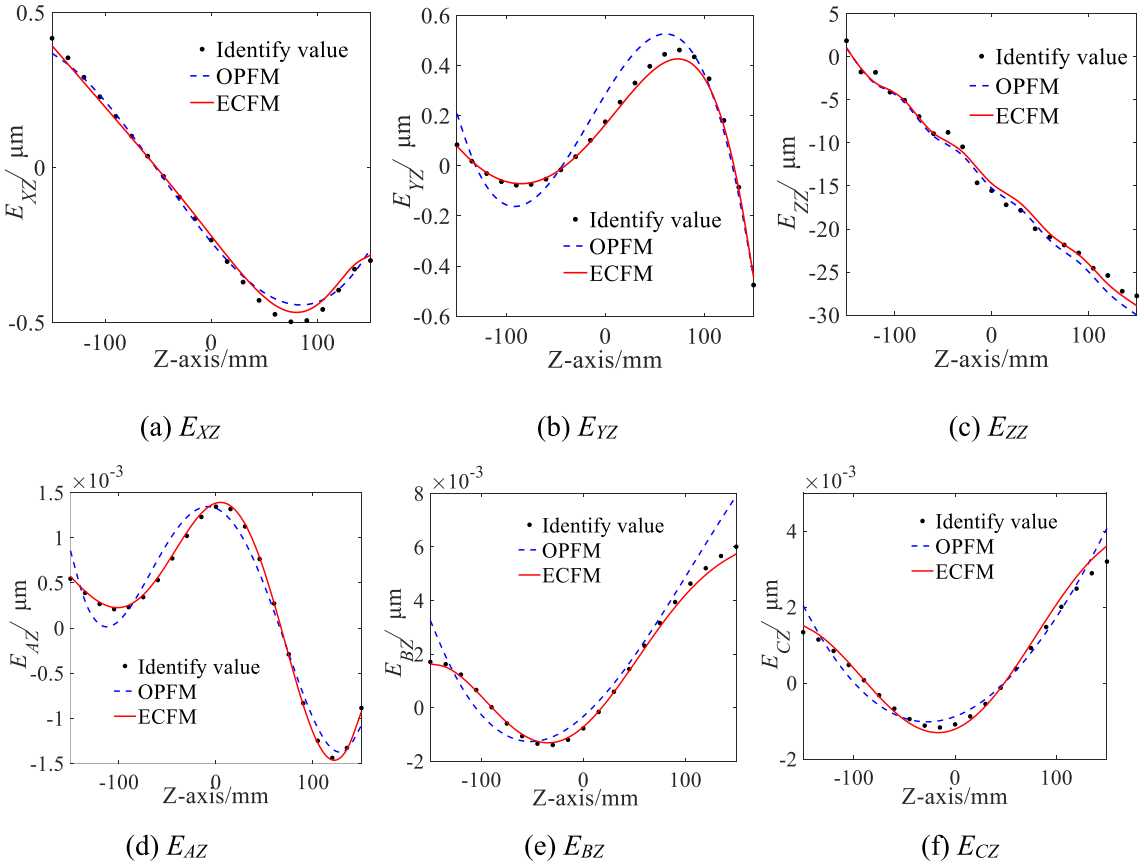

Fig. 12 Fitting cure of *Z*-axis geometric error

Fig. 13 Error compensation experiment

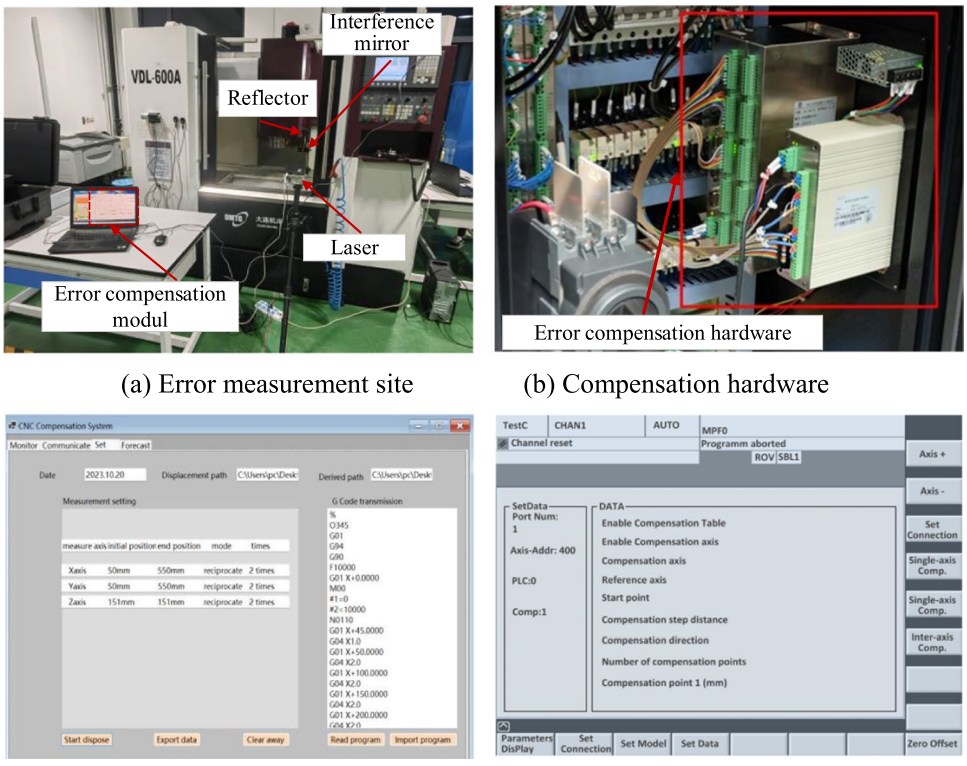

compensation upper computer. During the compensation of geometric errors, communication between the upper computer and the machine tool was established by configuring the IP address, as illustrated in Fig. 13. After the G-code file is executed, the compensation values are automatically generated by the upper computer and then transferred to the CNC system. Geometric error measurements and identification are carried out after the corresponding compensation parameters are configured.

The error curve before compensation is compared, as depicted in Fig. 14.

It can be seen from Fig. 14 that the positioning error curve exhibits a linear growth trend with increasing travel. The straightness error is impacted by the angle error of the workbench, resulting in a fluctuating curve along the reference line with a downward curved and wavy shape. The angle error curve does not exhibit linear characteristics but fluctuates with a trigonometric function before compensation. After compensation, the numerical range of various error curves is significantly reduced. The error data were analyzed and compared before and after compensation, as presented in Table 5.

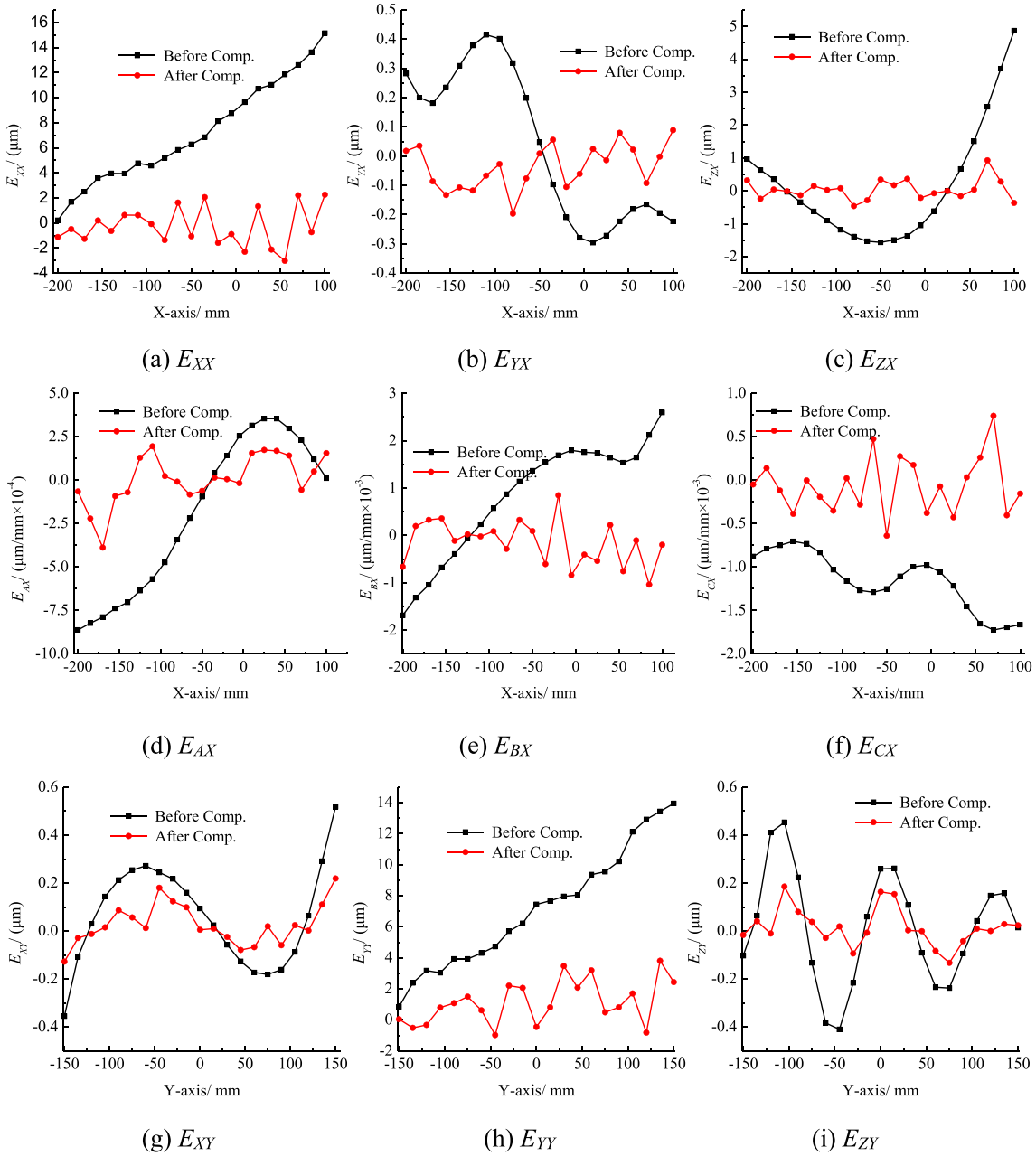

Fig. 14 Error curves before and after compensation

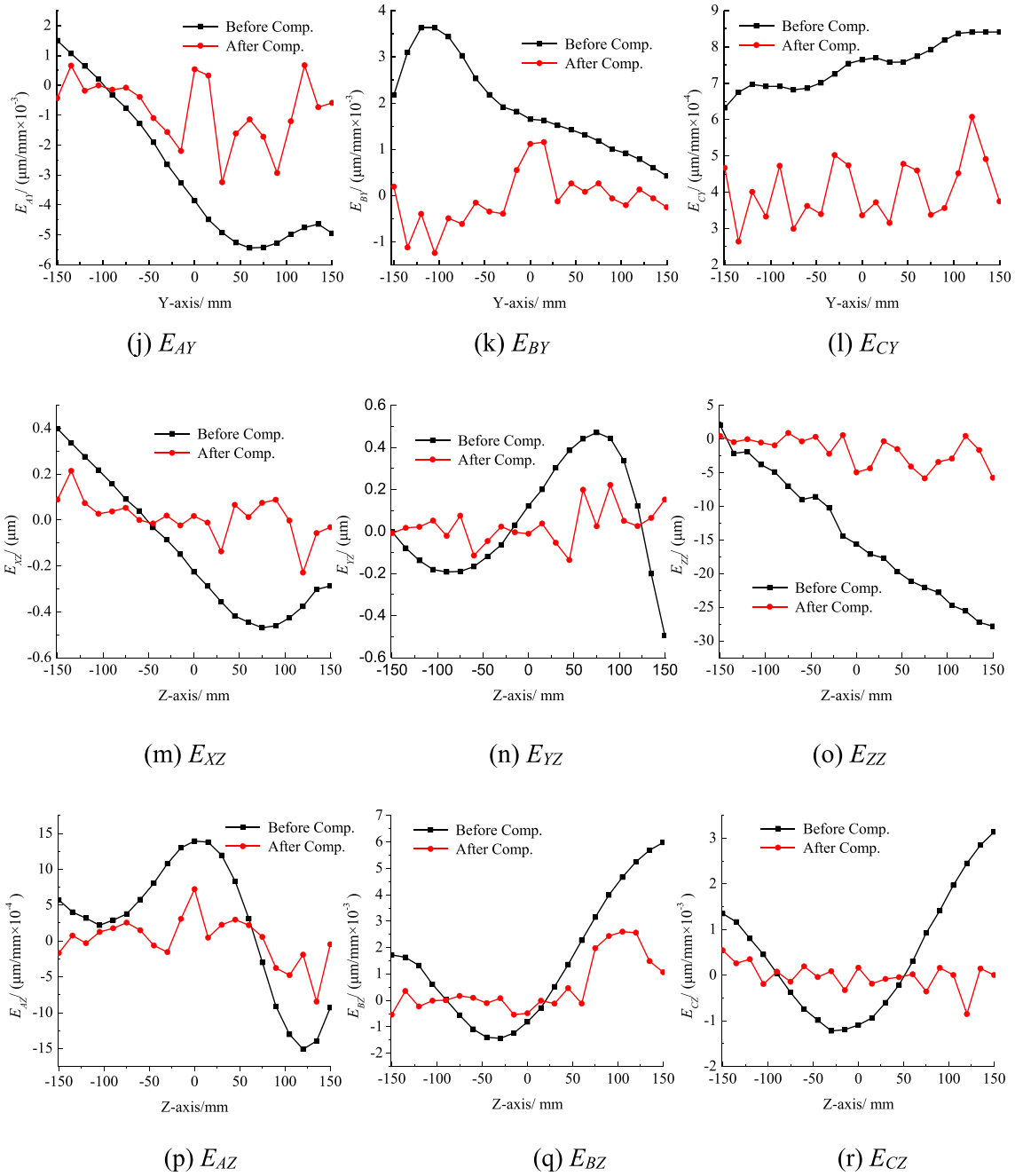

Fig. 14 (continued)

The results presented in Table 5 indicate a significant reduction in positioning error, straightness error, angle error, and verticality error values after compensation. The geometric errors in the X, Y, and Z directions have decreased by an average of 69.7%, demonstrating high compensation accuracy across the entire measurement range.

To further validate the effectiveness of error compensation, a double ball bar (DBB) was employed to conduct a 360° standard circular trajectory test on the XOY plane both before and after compensation. Additionally, a 220° standard circular trajectory test was performed on the XOZ and YOZ planes. The testing parameters included a radius of 100 mm and a feed rate of 200 mm/min, as depicted in Fig. 15.

Table 5 Comparison of error data before and after compensation

Error terms	Values before compensation	Values after compensation	Ratio improvement
E_{XX}/(μm)	7.645	2.547	66.7%
E_{YY}/(μm)	6.496	1.980	69.5%
E_{ZZ}/(μm)	14.360	2.766	80.7%
E_{YX}/(μm)	0.289	0.043	85.1%
E_{ZX}/(μm)	1.418	0.296	79.1%
E_{XY}/(μm)	0.172	0.059	65.7%
E_{ZY}/(μm)	0.211	0.065	69.2%
E_{XZ}/(μm)	0.277	0.060	78.3%
E_{YZ}/(μm)	0.220	0.063	71.4%
E_{AX}/(μm/mm)	0.0004	0.0002	50.0%
E_{CX}/(μm/mm)	0.0011	0.0002	81.2%
E_{BX}/(μm/mm)	0.0012	0.0004	66.7%
E_{CY}/(μm/mm)	0.0007	0.0004	42.9%
E_{BY}/(μm/mm)	0.0019	0.0004	78.9%
E_{AY}/(μm/mm)	0.0032	0.0010	68.8%
E_{BZ}/(μm/mm)	0.0021	0.0006	71.4%
E_{AZ}/(μm/mm)	0.0008	0.0002	75.0%
E_{CZ}/(μm/mm)	0.0012	0.0002	83.3%
E_{C0X} (μm/m)	30.714	3.912	87.3%
E_{A0Z} (μm/m)	−47.365	−28.245	40.4%
E_{B0Z} (μm/m)	51.872	23.705	54.3%

trajectory. A detailed comparison of the circular trajectories before and after compensation is provided in Table 6.

The compensability of the error term may decrease due to the resolution limitations of the numerical control system. Interestingly, the improvement of roundness error in the YOZ plane surpasses that in both the XOY and XOZ planes. On average, the roundness error compensation rate stands at 68.7%, indicative of a notable enhancement in the accuracy of two-axis synchronous motion.

To validate the effectiveness of the method proposed in this paper for enhancing overall machine accuracy, error compensation was conducted both with and without spatial error compensation enabled. Polynomial fitting was employed to represent the error terms proposed on a trial standard specimen. The specimen used conforms to the machined workpiece specified in ISO 10791–2020, as depicted in Fig. 17.

During clamping, the workpiece is approximately positioned at the midpoint of the *X*-axis and *Y*-axis travel and is secured using a dedicated fixture to ensure maximum stability of the tool and fixture. Following installation, the parallelism between the mounting surface and the clamping surface of the fixture is inspected to ensure the flatness of the fixture and workpiece mounting surfaces. To secure the workpiece, countersunk screws are used to prevent interference between the tool and the screws. A 32-mm diameter end mill is employed for machining all external surfaces of the workpiece, with cutting parameters set at a

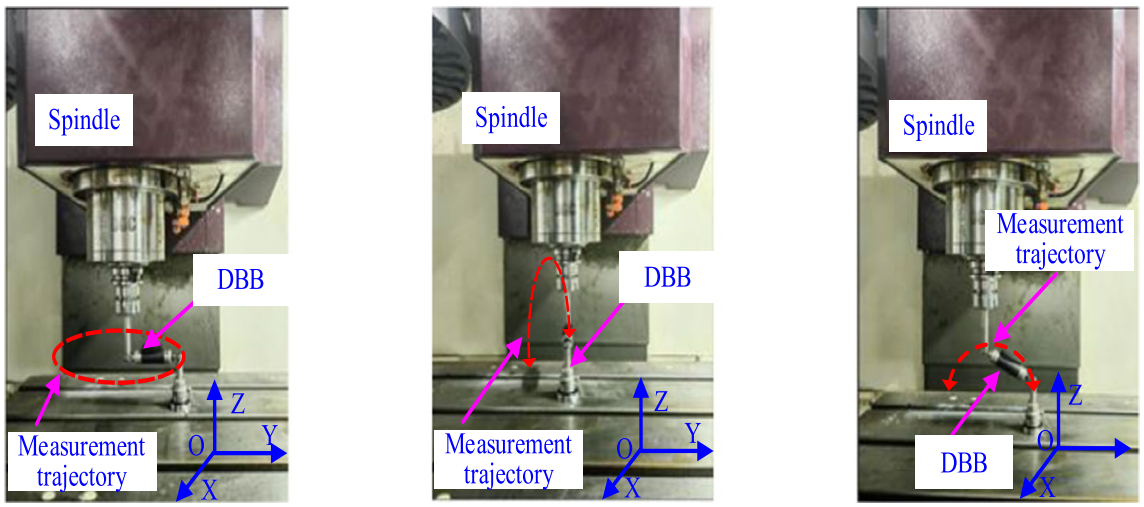

(a) XOY plane (b) YOZ plane (c) XOZ plane

Fig. 15 Measurement in three planes with DBB

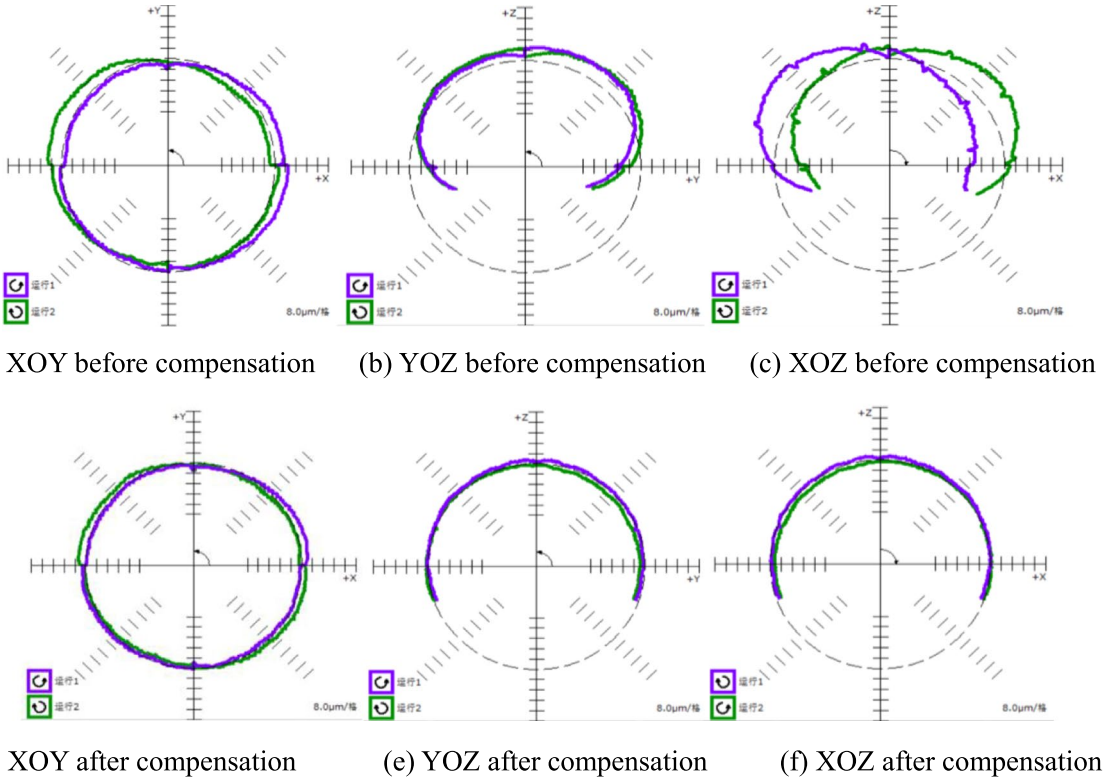

(a) XOY before compensation (b) YOZ before compensation (c) XOZ before compensation

(d) XOY after compensation (e) YOZ after compensation (f) XOZ after compensation

Fig. 16 Comparison of circular trajectories compensates

Table 6 Comparison of circular trajectory before and after compensation

Measuring plane	Roundness before comp	Roundness with comp	Proportion
XOY	16.5 μm	10.8 μm	34.5%
YOZ	46.2 μm	6.6 μm	85.7%
XOZ	48.0 μm	6.7 μm	86.0%

cutting speed of 50 mm/min, a feed rate of 0.05 mm/tooth, and a radial depth of cut of 0.2 mm. The cutting process of the specimen is illustrated in Fig. 18.

The feature accuracy of the specimen is inspected on CMM after machining is completed, and the inspection results are presented in Table 7. Table 7 reveals that the feature accuracy of the machined specimen is superior after

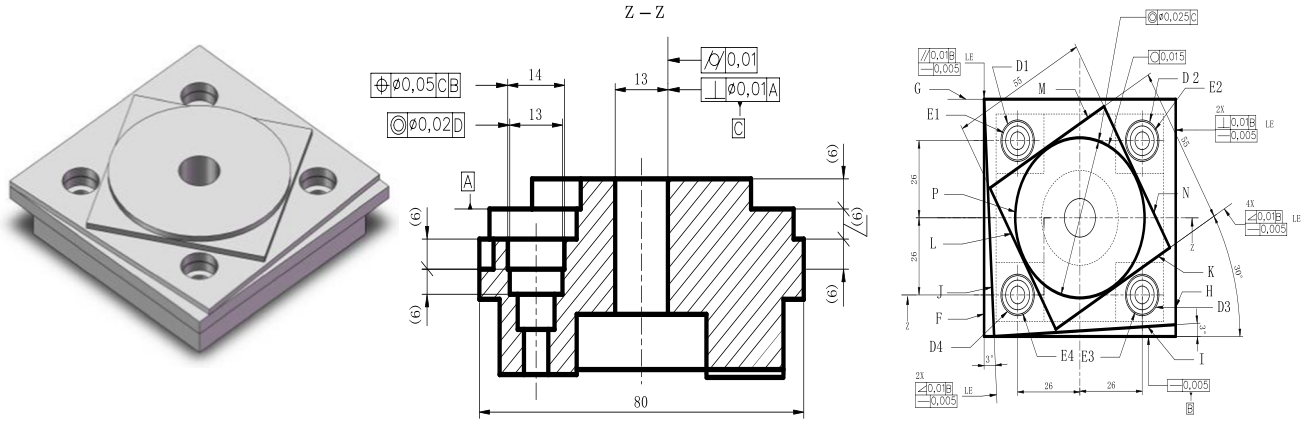

(a) 3D model (b) Front view (c) Top view

Fig. 17 Model and tolerances of piece

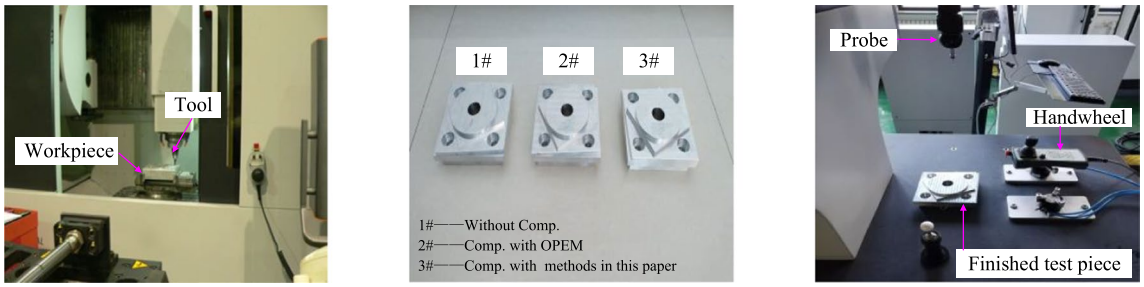

(a) Cutting of piece test (b) Finished test pieces (c) Aaccuracy measurement

Fig. 18 Cutting of piece test and accuracy measurement

Table 7 The tolerances of piece test before and after compensation (dimensions in mm)

Measurement indicators	Tolerance	Without Comp	Comp. with OPEM	Comp. with the proposed method
Centre hole: Cylindricity	0.01	0.008	0.006	0.005
Centre hole: Squareness of the hole axis to datum A	0.01	0.007	0.004	0.003
Straightness of the square edge	0.01	0.006, 0.007, 0.009, 0.01	0.004, 0.005, 0.006, 0.008	0.003, 0.004, 0.004, 0.004
Squareness of adjacent edges of the square to datum B	0.013	0.009	0.006	0.003
Tilt of the four edges of the rhombus to datum B	0.013	0.008	0.006	0.004
Roundness	0.016	0.0012	0.010	0.006
Concentricity of the outer circle with center hole C	Φ0.016	Φ0.013	Φ0.011	Φ0.008

spatial error compensation compared to before compensation, implementing error compensation using orthogonal polynomials resulted in an improvement range of [15.4%, 33.3%] in the accuracy of the test specimen, with an average improvement ratio of 25.9%.

In the XOY plane under quasi-static conditions, the improvement ratio after compensation for a circular trajectory is 34.5%. In contrast, the roundness error improvement ratio for standard test pieces under cutting conditions is 62.5%. The primary reason for this disparity is that the error compensation in the XOY plane only addresses the errors of the *X*- and *Y*-axes, while under cutting conditions, compensation is applied to all three linear axes' geometric errors. Thus, from the perspective of compensation effects within a single XOY plane, the accuracy improvement under quasi-static conditions surpasses that under cutting conditions. However, the form and position errors of machined parts reflect the combined effects of machine tool geometric errors, cutting forces, and servo system errors. In quasi-static DBB trajectory measurements, there is no error influence from cutting, leading to a higher average accuracy improvement under quasi-static conditions compared to that of machined parts.

6 Conclusion

This paper introduces a novel approach for modeling, measuring, identifying, and expressing geometric errors in multi-axis machine tools. The key innovation lies in leveraging dual quaternions theory to formulate a comprehensive volumetric error model. This method enables the selection of optimal measurement times, reduction of disturbance information and uncertainty, and the establishment of a parametric model for geometric errors with universal representation. The conclusions drawn from this study are as follows:

1. A comprehensive model is developed using dual quaternion theory to characterize the correlation between geometric error terms and spatial error vectors. The PIGEs of rotary and linear axes are redefined by employing the dual quaternion space transformation rule. The method of geometric error modeling based on dual quaternions enables singularity-free spatial transformations in Euclidean space, with its structure being simple, compact, and effectively avoiding multiplication operations between error term matrices.

2. The minimum number of measurement poses was determined using the iterative updating of the singular value of the error identification matrix. The optimal measurement point selection was conducted based on the improved Detmax algorithm of "replacement and addition." In the measurement of straightness error, variations in the position of the interferometer or reflector have been accounted for by employing different expressions to unify the identification results, which expands the applicability of the proposed method.
3. A parametric modeling method based on exponential cosine fitting is proposed, the ISSA-nested parametric uncertainty optimization approach was established, and the parametric errors of geometric error terms with inadequate fitting effects are effectively modeled.
4. An experiment involving the measurement and compensation of geometric errors in a multi-axis machine tool was conducted using an error compensation system. Following the compensation process, the mean values of geometric errors in the X, Y, and Z directions exhibited a remarkable reduction of 69.7%. Moreover, the accuracy of two-axis synchronous motion witnessed a substantial improvement increasing by 68.7%.

Despite the progress, it should be pointed out that thermal errors as another significant factor of quasi-static errors collectively influence the accuracy of machine tools along with geometric errors. Therefore, the coupling effect between geometric errors and thermal errors needs to be further addressed, which is of more practical significance.

Author contribution Shijie Guo did the methodology research and formal analysis and wrote the original draft. Yunhe Zou did the measurement experiment and data analysis. Wangwang Huang did the conceptualization, experiment, and writing. Shufeng Tang did the experiment, and Xuesong Mei did the review.

Funding This research was supported by the National Natural Science Foundation of China (Grant no. 52065053, 52365064, 52365058), the Key Technological Project of Inner Mongolia of China (Grant no. 2021GG0255), the Program for Innovative Research Team in Universities of Inner Mongolia Autonomous Region of China (Grant no. NMGIRT2213), the Science and Technology Development Special Project of Central Guide the Local Government of China (Grant no. 2020ZY0002), the Natural Science Foundation of Inner Mongolia Autonomous Region of China (Grant no. 2023LHMS05017 and 2023LHMS05018), the National Key R&D Program of China (Grant no. 2018YFB1307501), and the Program for Young Talents of Science and Technology in Universities of Inner Mongolia Autonomous Region (NJYT23043).

Data availability The datasets used or analyzed during the current study are available from the corresponding author on reasonable request.

Code availability The code generated or used during the current study is available from the corresponding author on reasonable request.

Declarations

Ethics approval This paper is compliant with the ethical standard.

Consent to participate All the participants provided informed consent.

Consent for publication Informed consent for publication was obtained from all participants.

Competing interests The authors declare no competing interests.

References

1. Chen L, Xu H, Huang Q, Wang P (2024) An integrated method for compensating and correcting nonlinear error in five-axis machining utilizing cutter contacting point data. Sci Rep-UK 14(1):8763
2. Yue C, Gao H, Liu X, Liang SY, Wang L (2019) A review of chatter vibration research in milling. Chinese J Aeronau 32(2):215–242
3. Zhang Z, Jiang F, Luo M, Wu BH, Zhang DH, Tang K (2024) Geometric error measuring, modeling, and compensation for CNC machine tools: a review. Chinese J Aeronau 37(2):163–198
4. Ma C, Gui H, Liu JL (2023) Self learning-empowered thermal error control method of precision machine tools based on digital twin. J Intell Manuf 34(2):695–717
5. Yang Y, Lv J, Xiao YK, Feng XB, Du ZC (2023) Enhanced modeling method of thermal behaviors in machine tool motorized spindles based on the mixture of thermal mechanism and machine learning. J Intell Manuf. https://doi.org/10.1007/s10845-023-02234-w
6. Onishi S, Ibaraki S, Kato T, Yamaguchi M, Sugimoto T (2022) A self-calibration scheme to monitor long-term changes in linear and rotary axis geometric errors. Measurement 196:111183
7. Ding S, Zhang X, Chen Z, Wu WW (2023) Position-independent geometric error compensation of a non-orthogonal five-axis machine tool using a simplified algebraic algorithm. Proc Inst-Mech Eng B J Eng Manuf. https://doi.org/10.1177/09544054231205140
8. Guo SJ, Si ZX, Sa RN, Zou YH, and Mei XS (2024) Geometric error modeling and decoupling identification of rotary axis of five-axis machine tool based on spatial trajectory planning. Measurement 114887. https://doi.org/10.1016/j.measurement.2024.114887
9. ISO 10791–7 (2020) Test conditions for machining centers-part 7: accuracy of finished test pieces. ISO
10. Xiang ST, Altintas Y (2016) Modeling and compensation of volumetric errors for five-axis machine tools. Int J Mach Tools Manuf 101:65–78
11. Gao W, Ibaraki S, Donmez MA, Kono D, Mayer J, Chen Y, Szipka K, Archenti A, Linares JM, Suzuki N (2023) Machine tool calibration: measurement, modeling, and compensation of machine tool errors. Int J Mach Tools Manuf 187:104017
12. Osei S, Wei W, Yu J, Ding Q (2023) A new effective decoupling method to identify the tracking errors of the motion axes of the five-axis machine tools. J Intell Manuf. https://doi.org/10.1007/s10845-023-02220-2
13. Zhang ZL, Cai LG, Cheng Q, Liu ZF, Gu PH (2019) A geometric error budget method to improve machining accuracy reliability of multi-axis machine tools. J Intell Manuf 30(2):495–519
14. Ding S, Song Z, Chen Z, Wu W, Song A (2023) An efficient geometric error modelling algorithm of CNC machine tool without interference of higher-order error terms. Int J Adv Manuf Technol 126(7–8):3353–3366

15. Chen GD, Zhang L, Wang C, Xiang H, Tong GQ, Zhao DZ (2022) High-precision modeling of CNCs' spatial errors based on screw theory. SN Applied Sciences 4(2):45–59
16. Chen K, Liu S, Tian A, Mo W, Jin S (2023) Interaction analysis of geometric tolerance of multi-axis machine tools based on kinematic Jacobian-Torsor model. Proc InstMech Eng B J Eng Manuf 237(1–2):240–249
17. Yao SH, Huang H, Tian WJ, Gao WG, Weng L, Zhang DW (2023) Simultaneous identification for geometric error of dual rotary axes in five-axis machine tools. Measurement 220:113368
18. Fu GQ, Gong H, Fu JZ, Gao H, Deng XL (2019) Geometric error contribution modeling and sensitivity evaluating for each axis of five-axis machine tools based on POE theory and transforming differential changes between coordinate frames. Int J Mach Tools Manuf 147:103455
19. He ZY, Fu JZ, Zhang X, Shen HY (2016) A uniform expression model for volumetric errors of machine tools. Int J Mach Tools Manuf 100:93–104
20. Peng WC, Xia HJ, Chen XD, Lin ZQ, Wang ZF, Li HY (2018) Position-dependent geometric errors measurement and identification for rotary axis of multi-axis machine tools based on optimization method using double ball bar. Int J Adv Manuf Technol 99(9):2295–2307
21. Tian WJ, Yang G, Wang LN, Yin FW, Gao WG (2018) The application of a regularization method to the estimation of geometric errors of a three-axis machine tool using a double ball bar. J Mech Sci Technol 32:4871–4881
22. Fan KG, Yang JG, Yang LY (2014) Unified error model based spatial error compensation for four types of CNC machining center: part II-unified model based spatial error compensation. Mech Syst Signal Pr 49(1):63–76
23. Dantam NT (2021) Robust and efficient forward, differential, and inverse kinematics using dual quaternions. Int Journal Robot Res 40(10–11):1087–1105
24. Qi LQ, Ling C, Yan H (2022) Dual quaternions and dual quaternion vectors. Com Appl Math Comput 4(4):1494–1508
25. Breitzke A, Hintze W (2022) Workshop-suited geometric errors identification of three-axis machine tools using on-machine measurement for long term precision assurance. Precis Eng 75:235–247
26. Matsuzaki K, Takatsuji T, Sato O (2023) Evaluation and compensation of geometrical errors of X-ray computed tomography system using a laser tracking interferometer. Precis Eng 80:243–255
27. Zhang H, Xiang ST, Liu C, Sun J, Attifu JK (2023) Reverse identification of dynamic and static motion errors for five-axis machine based on specimen feature decomposition. Isa T 134:302–311
28. Zhang JY, Lou ZF, Fan KC, Zhang HP, Zhou JJ (2023) Development of a precision vertical planar stage as a programmable planar artefact. Measurement 217:113055
29. Cai YD, Wang LH, Liu Y, Li C, Fan KC (2022) Accuracy improvement of linear stages using on-machine geometric error measurement system and error transformation model. Opt express 30(5):7539–7550
30. Uekita M, Takaya Y (2016) On-machine dimensional measurement of large parts by compensating for volumetric errors of machine tools. Precis Eng 43:200–210
31. Maruyama D, Ibaraki S, Sakata R (2022) Measurement of machine tool two-dimensional error motions using direction-regulated laser interferometers. Int J Auto Tech 16(2):157–166
32. Ibaraki S, Hiruya M (2021) A novel scheme to measure 2D error motions of linear axes by regulating the direction of a laser interferometer. Precis Eng 67:152–159
33. Peng WC, Huang JF, Long DF, Zeng DC, Xia HJ (2023) Measurement and identification method for geometric errors of the linear axis based on laser interferometer optimal measurement parameters method. P I Mech Eng C: J Mech 237(17):4051–4061
34. Zhang XQ, Chen GD, Zhang L, Hu YW, Mao J, Zhang ZY (2023) Modeling of CNC machine tools' spatial geometric error based on two-dimensional angle error. SN Appl Sci 5(1):1–10
35. Tang ZW, Zhou YS, Wang SL, Zhu J, Tang JY (2022) An innovative geometric error compensation of the multi-axis CNC machine tools with non-rotary cutters to the accurate worm grinding of spur face gears. Mech Mach Theory 169:104664
36. Zhong XM, Liu HQ, Mao XY, Li B, He SP (2019) Influence and error transfer in assembly process of geometric errors of a translational axis on volumetric error in machine tools. Measurement 140:450–461
37. Brosed FJ, Aguilar JJ, Acero R, Santolaria J, Aguado S, Pueo M (2022) Calibration and uncertainty budget analysis of a high precision telescopic instrument for simultaneous laser multilateration. Measurement 190:110735
38. Zhou R, Kauschinger B, Ihlenfeldt S (2020) Path generation and optimization for DBB measurement with continuous data capture. Measurement 155:107550
39. Wang H, Jiang XG (2023) Identification and compensation of position independent geometric errors of dual rotary axes for hybrid-type five-axis machine tool based on unit dual quaternions. Measurement 211:112587
40. Yang SH, Lee KI (2024) Adaptive identification of the position-independent geometric errors for the rotary axis of five-axis machine tools to directly improve workpiece geometric errors. Int J Precis Eng Man 25:995–1010
41. Xu K, Zhuang ZX, Ji YL, Xu JH, Yu YB, Bi QZ (2024) An efficient method for measuring and identifying geometric and dynamic errors in dual five-axis machine tools. Precis Eng 86:359–375
42. Xu K, Li GL, He K, Tao XH (2020) Identification of position-dependent geometric errors with non-integer exponents for linear axis using double ball bar. Int J Mech Sci 170:105326
43. ISO 230–1 (2012) Test code for machine tools-part 1: Part 1: Geometric accuracy of machines operating under no-load or quasi-static conditions. ISO
44. Guo SJ, Tang SF, Wu JX, Qiao G (2022) All position-independent and position-dependent geometric error measurement and identification of the precision of a horizontal boring machine tool. Int J Adv Manuf Technol 121(9):6453–6473